Original Paper

Integrated modeling of fracturing-flowback-production dynamics and calibration on field data: Optimum well startup scenarios

S.A. Boronin [a, *], K.I. Tolmacheva [a], I.A. Garagash [a, c], I.R. Abdrakhmanov [a], G. Yu Fisher [a], A.L. Vainshtein [a], P.K. Kabanova [b], E.V. Shel [b], G.V. Paderin [b], A.A. Osiptsov [a]

[a] Skolkovo Institute of Science and Technology (Skoltech), Russia
[b] LLC Gazpromneft Science and Technology Center, Russia
[c] The Schmidt Institute of Physics of the Earth of the Russian Academy of Sciences, Moscow, Russia

ARTICLE INFO

ABSTRACT

We aim at the development of a general modelling workflow for design and optimization of the well flowback and startup operation on hydraulically fractured wells. Fracture flowback model developed earlier by the authors is extended to take into account several new fluid mechanics factors accompanying flowback, namely, viscoplastic rheology of unbroken cross-linked gel and coupled "fracture-reservoir" numerical submodel for influx from rock formation. We also developed models and implemented new geomechanical factors, namely, (i) fracture closure in gaps between proppant pillars and in proppant-free cavity in the vicinity of the well taking into account formation creep; (ii) propagation of plastic deformations due to tensile rock failure from the fracture face into the fluid-saturated reservoir.

We carried out parametric calculations to study the dynamics of fracture conductivity during flowback and its effect on well production for the set of parameters typical of oil wells in Achimov formation of Western Siberia, Russia. The first set of calculations is carried out using the flowback model in the reservoir linear flow regime. It is obtained that the typical length of hydraulic fracture zone, in which tensile rock failure at the fracture walls occurs, is insignificant. In the range of rock permeability in between 0.01 mD and 1 D, we studied the effect of non-dimensional governing parameters as well as bottomhole pressure drop dynamics on oil production. We obtained a map of pressure drop regimes (fast, moderate or slow) leading to maximum cumulative oil production. The second set of parametric calculations is carried out using integrated well production modelling workflow, in which the flowback model acts as a missing link in between hydraulic fracturing and reservoir commercial simulators. We evaluated quantitatively effects of initial fracture aperture, proppant diameter, yield stress of fracturing fluid, pressure drop rate and proppant material type (ceramic and sand) on long-term well production beyond formation linear regime. The third set of parametric calculations is carried out using the flowback model history-matched to field data related to production of four multistage hydraulically fractured oil wells in Achimov formation of Western Siberia, Russia. On the basis of the matched model we evaluated geomechanics effects on fracture conductivity degradation. We also performed sensitivity analysis in the framework of the history-matched model to study the impact of geomechanics and fluid rheology parameters on flowback efficiency.

1. Introduction

Flowback from hydraulically fractured wells drilled in a hydrocarbon-bearing formation is becoming a subject of intensive research over the last five years. Increasing attention to this topic is due to the industry trends since 2014 focused on cost efficiency and CapEx optimization. The added value created during massive multistage fracturing treatment is often lost during aggressive fracture flowback and well startup, hence service companies and operators pay more attention these days to a more careful approach to optimized procedures of fracture flowback called for saving the

* Corresponding author.
  E-mail address: sergeyboronin@yandex.ru (S.A. Boronin).

conductive paths created during fracturing for hydrocarbons transport from the far-field reservoir to the well and then to surface (Potapenko et al., 2017, 2019, 2020). Operational optimization of oilfield technologies (including flowback) gains significant interest worldwide in view of recently formulated governmental strategies on energy transition and reduction of carbon footprint.

Usually, the process of fracture creation and propagation and proppant placement is carefully designed with the help of simulators of hydraulic fracturing based on advanced continuum mechanics models: comprehensive review into computer simulation of hydraulic fractures is summarized in Adachi et al. (2007) along with the two most recent updates with the focus on fluid mechanics aspect (Osiptsov, 2017) and numerical algorithms (Lecampion et al., 2018). The subsequent long term production is also thoughtfully planned with the help of 3D reservoir simulators. At the same time, there is relatively short operation (on the time scale of long-term production), called flowback, which importance has long been underestimated. By flowback we understand the process of cleanup of the "well-multiple fractures" system to set up the well for steady-state production after cleanup is complete.

A rate transient model for describing the fracturing fluid flowback was presented in Abbasi et al. (2012). Effect of proppant distribution in a fracture on the overall fracture conductivity has been studied by Wang and Elsworth (2018), Wang et al. (2018). There is a body of literature focused specifically on elasticity problem of fracture closure during flowback (e.g., flowback from fracture network during closure was studied in Dana et al. (2018) and various modes of closure for a single fracture were considered in Dahi Taleghani et al. (2020)). Proppant flowback model is developed and validated against a set of laboratory experimental data by Chuprakov et al. (2020, 2021). Critical filtration velocity for proppant pack mobilization was derived and validated as a function of particle size and cohesion, wall roughness and softness. A comprehensive review on proppant embedment during shale gas fracturing can be found in Katende et al. (2021). A model for fracture closure in between proppant pillars is formulated by Skopintsev et al. (2022) assuming elastic rock deformation and incompressible proppant pack. Effects of surfactants on flowback efficiency is investigated in Wijaya and Sheng (2020). The concept of zero flowback rate has been proposed and studied in You et al. (2021) for the shale gas fracture flowback, with the aim to maximize production.

Integrated design of fracturing-flowback-production is being discussed in a chain of papers (Potapenko et al., 2017, 2020, 2019; Chuprakov et al., 2020). Coupled simulations of dynamic interactions between the well, hydraulic fractures and reservoir have been studied by Aksenov et al. (2021) with the focus on performance of numerical simulations. Accelerated Anderson and Aitken fixed-point algorithms were considered, and recommendations for the choice of the particular algorithm and tunable relaxation parameter were proposed. An interesting concept of cascading failure of the fracture system during aggressive flowback was proposed and discussed by Chertov and Sinkov (2020).

A rigorous coupled flow-geomechanics semianalytical approach to analyze flowback data and forecast production performance in multifractured horizontal wells is presented in Lamidi and Clarkson (2022) and Fu and Dehghanpour (2022). Flowback, post-flowback and completion-design data of 19 multi-fractured horizontal wells (MFHWs) completed in Niobrara and Codell formations has been analyzed in Moussa et al. (2022). The impact of capillary pressure and flowback operational variables on hydraulically fractured tight gas wells was studied in Verdugo and Doster (2022) with the objective of understanding the clean-up process at reservoir level and its impact on future well performance. Through numerical reservoir simulation, different scenarios were investigated, varying capillary pressure, flowback duration, shut-in duration and drawdown. These scenarios are interpreted with rate transient analysis. The results of this work show the ambivalent effect of capillary pressure in terms of facilitating imbibition but also holding back water close to the fracture. The novelty of this work consists in the findings that for lower capillary pressures, short shut-in periods lead to a better well productivity while for higher capillary pressure extended shut-in periods are better for well productivity.

A more detailed review on the papers devoted to flowback published before 2019 can be found in the previous study by Osiptsov et al. (2020) and in the papers cited therein.

This work is a continuation of our study with the focus on expansion of the geomechanics/fluid mechanics effects in the fracture conductivity model during flowback, integration of the fracture flowback model with a fracture design and long-term production simulators (as shown in Fig. 1) as well as history matching of the developed flowback model to field data of four multistage hydraulically fractured oil wells in Achimov terrigenous formation of Western Siberia, Russia. Field testing campaign was discussed in Osiptsov et al. (2019), Vainshtein et al. (2020, 2021).

Mathematical model of fracture cleanup and flowback presented in our previous paper (Osiptsov et al., 2020) is extended to include the effect of yield stress of fracturing fluid (unbroken crosslinked gel typically used to create hydraulic fractures in traditional rock formations), improved description of influx from reservoir into the fracture, and several new geomechanical effects, namely, fracture closure in between proppant pillars and formation of plastic deformation zone at the fracture walls due to tensile rock failure.

More recently, the study (Zhang and Emami-Meybodi, 2022b) presents a new type-curve method to characterize hydraulic fracture (HF) attributes and dynamics by analyzing two-phase flowback data from multi-fractured horizontal wells. The proposed method is applied to two multistage hydraulically fractured wells in Marcellus shale gas and Eagle Ford shale oil. The papers Zhang and Emami-Meybodi (2022a, 2020b) present a new semi-analytical method to simulate the two-phase liquid transport in hydraulic fractures (HF) and matrix system, which can be applied to characterize HF attributes and dynamics using the flowback data from hydraulically fractured shale oil wells. The work Zhang and Emami-Meybodi (2021) develops a new semi-analytical method to estimate HF attributes for shale gas wells exhibiting two-phase flow based on straight line analysis. The proposed method considers two-phase infinite acting linear flow (IALF) and boundary dominated flow (BDF) for both HF and matrix domains. In addition, matrix flow considers desorption, diffusion, slip flow, continuum flow, stress dependence rock, and adsorbed water film in the nanopores. Two multiphase flowback models for gas and water phase are constructed in Zhang and Emami-Meybodi (2020a) under boundary dominated flow (BDF) condition by considering gas influx from matrix. In addition, a workflow is proposed to quantitatively evaluate hydraulic fracture closure and fracture properties using both water-phase and gas-phase flowback data. In Zhang and Taleghani (2022), an integrated numerical model is proposed to simulate fracture propagation, well shut-in and finally flowback from fracture network in shales. To simulate the fracture propagation with branches, a cohesive zone model with node displacement is adopted. During fracture closure process, proppant stress is integrated to consider the presence of proppants and non-linear fracture permeability evolution is also considered to represent the transition from fracture flow to Darcy's flow. The work Jia et al. (2022) considered a new coupled flow-geomechanical model to study the dynamic behavior of unpropped and propped fractures of fractured horizontal wells in shale gas reservoir during two-phase flowback and production. In the experimental study Guo et al.
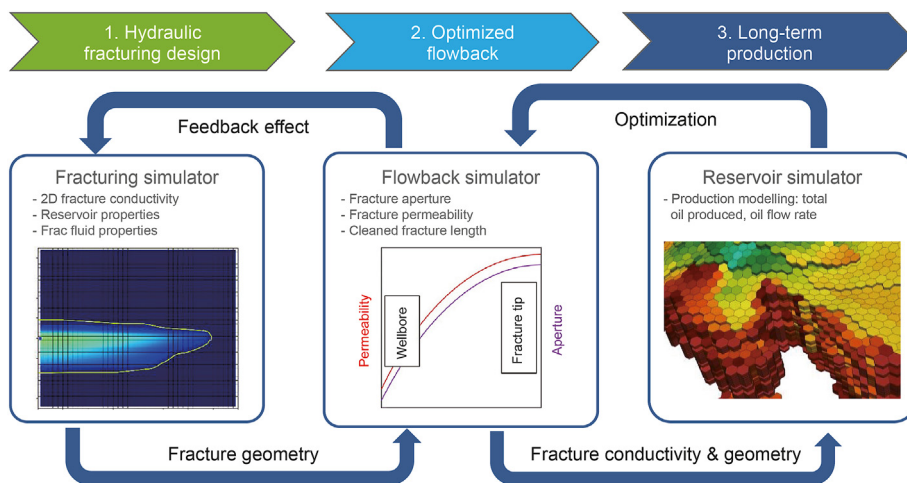
Fig. 1. Integrated modelling framework.

(2022), steel plates and hydraulically fractured reservoir rocks are tested in a modified API cell to understand the impacts of flowback rate, fracturing fluid, and closure stress on proppant flowback and fracture conductivity.

These papers have been focused primarily on shales formations, and hence, there is still room for development of integrated flowback models tied to the specifics of Achimov formations, which are low perm but conventional.

This paper is organized as follows: Section 2 presents geomechanics models of various processes accompanying fracture flowback including fracture conductivity degradation during flowback with account for fracture closure in between proppant pillars with rock creep; in Section 3 we present the fluid mechanics model of fluid/fluid displacement in a proppant-filled fracture during flowback and results of parametric study of production with respect to variation in non-dimensional governing parameter and parametric study of flowback integrated into well production modelling workflow; Section 4 covers adaptation of the fracture flowback model to field data collected from four oil wells in Achimov formation located in Western Siberia, Russia. Conclusions and recommendations for future work are given in Section 5.

2. Geomechanics models for fracture flowback

In this section we present a chain of geomechanics models covering the phenomena peculiar to the process of fracture closure on proppant during flowback and well startup: rock creep during closure on pillars and stress variation in the rock near fracture surface.

2.1. Fracture closure on proppant pillars with effects of rock creep

One of the contemporary variants of hydraulic fracturing technology is based on the so-called alternate slug fracturing (d'Huteau et al., 2011), where pulses of clean fluid are interchanging with pulses of proppant-laden suspension while pumping from surface, which results in heterogeneous proppant placement downhole. Eventually the fracture is filled with an array of proppant pillars surrounded by particle-free channels. Effective height-averaged conductivity of such system is orders of magnitude higher that that of a fracture homogeneously filled with proppant. At the same time, transient dynamics during flowback and well startup may damage this excessive conductivity due to partial closure of open fracture channels between pillars.

2.1.1. Fracture closure on proppant pillars in linear configuration

We consider the process of fracture closure between proppant pillars (yellow domain in Fig. 2) in the absence of rock creep assuming linear problem configuration and plane strain approach. During flowback, the pressure in the fracture p_{si} is gradually decreasing, starting from the value of the fracture propagation pressure $p_{si} = p_h$ and attaining the pore pressure $p_{si} = p_r$. As a result of pressure drop $(p_h - p_{si})$, the proppant is packed and an effective medium is formed (Fig. 3). With a decrease in fluid pressure in the fracture, the confinement stress applied to proppant pillars from the fracture faces increases, which leads to a plastic deformation of effective medium at the boundaries of pillars/open channels in the zones of stress concentration (Fig. 4). Transition to plasticity occurs when the compression strength limit is attained σ_{st}.

Let the x_2-axis be directed perpendicular to the fracture plane, while the x_1- and x_3-axes be in the fracture plane (Fig. 4). The stresses within proppant are given by $\sigma_{22}^{ini} = -(p_h - p_r)$ and $\sigma_{11} \ll \sigma_{22}$. Further the pore pressure is decreased by the magnitude
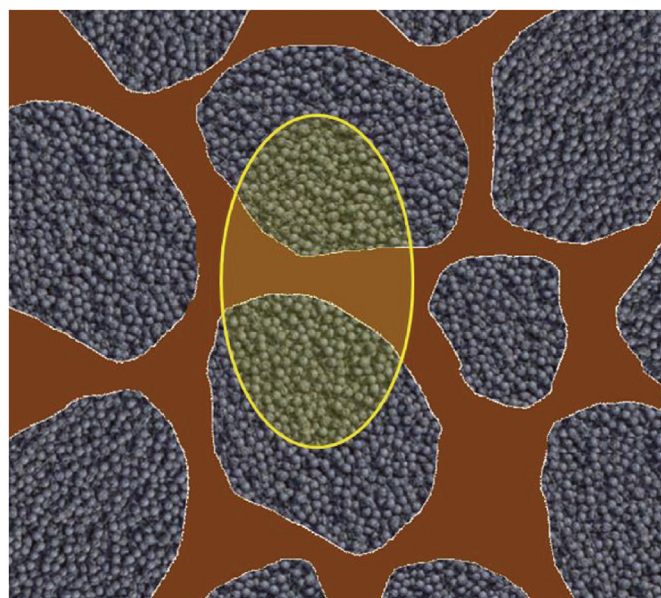

Fig. 2. Sketch of the heterogeneous proppant placement after alternate-slug fracturing with proppant pillars and particle-free channels.
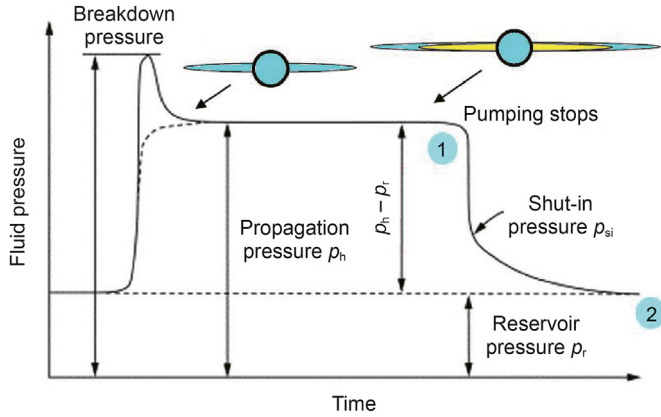
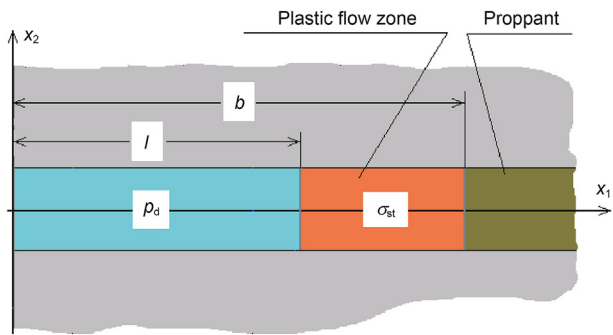**Fig. 3.** Pressure evolution during fracture initiation, propagation and closure.

Fig. 4. Loading of proppant pillars.

of Δp_d and the stress acting on proppant becomes equal to $p_d = (p_h - p_r) + \Delta p_d$.

We use the Prandtl-Reuss equations for a medium with internal friction and dilatancy. These equations relate the components of stress increments $d\sigma_{ij}$ with the components of the deformation tensor increments $d\epsilon_{ij}$ (Rudnicki and Rice, 1975):

$$d\sigma_{ij} = E_{ijkl}d\epsilon_{kl}. \qquad (1)$$

Coefficients E_{ijkl} in constitutive relations defined by Eq. (1) have a form:

$$E_{ijkl} = G\left\{ \left[\delta_{ik}\delta_{jl} + \delta_{il}\delta_{kj} + \left(\frac{K}{G} - \frac{2}{3}\right)\delta_{kl}\delta_{ij} \right] - \frac{G}{H + G + \alpha\Lambda K}\left(\frac{s_{ij}}{T} + \frac{K}{G}\Lambda\delta_{ij}\right)\left(\frac{s_{kl}}{T} + \frac{K}{G}\alpha\delta_{kl}\right) \right\}, \qquad (2)$$

where G is shear modulus; K is the bulk modulus; H is the plastic strengthening modulus; α is the internal friction coefficient; and Λ is the dilatancy coefficient.

Plastic flow of the medium is determined by the deviatoric part of the stress tensor $s_{ij} = \sigma_{ij} - \delta_{ij}\sigma$, mean stress $\sigma = \sigma_{ii}/3$ and the shear stress intensity (second invariant) $T = \sqrt{s_{ij}s_{ij}/2}$. The condition for plastic flow to occur is due to the Drucker-Prager criterion:

$$T + \alpha\sigma^{\text{eff}} = c, \qquad (3)$$

where c is cohesion, and

$$\sigma_{ij}^{\text{eff}} = \sigma_{ij} + (p_r - \Delta p_d)\delta_{ij}, \quad \sigma^{\text{eff}} = \frac{1}{3}\sigma_{ii}^{\text{eff}}.$$

We will assume that the stress state of proppant near the open channel is uniaxial, $d\sigma_{11} = d\epsilon_{33} = 0$ and plastic strengthening modulus of the pack is zero $H = 0$. In this case, according to constitutive relationships defined by Eq. (1), we write:

$$d\sigma_{22}^{\text{eff}} = E_{2222}^* d\epsilon_{22}, \qquad (4)$$

with

$$E_{2222}^* = E_{2222} - E_{2211}\frac{E_{1122}}{E_{1111}}.$$

In our case

$$T = \frac{1}{\sqrt{3}}|\sigma_{22}^{\text{eff}}|, \quad s_{22} = \frac{2}{3}\sigma_{22}^{\text{eff}}, \quad s_{11} = -\frac{1}{3}\sigma_{22}^{\text{eff}}.$$

Expressions for coefficients in Eq. (4) are formulated in Appendix 2.

Since the stress state in proppant varies proportionally to a single parameter Δp_d, the loading is a uniaxial and Eq. (4) can be rewritten in the form of an algebraic formula:

$$\sigma_{22}^{\text{eff}} = E_{2222}^* \epsilon_{22}. \qquad (5)$$

We assume that at the beginning of flowback the cohesion c consists the initial cohesion c_0 and the term $\alpha(p_h - p_r)/3$ due to proppant particle compaction, so the Drucker-Prager criterion defined by Eq. (3) can be written as:

$$|\sigma_{22}^{\text{eff}}| + \frac{\alpha}{\sqrt{3}}\sigma_{22}^{\text{eff}} = \sqrt{3}\left[c_0 + \frac{\alpha}{3}(p_h - p_r)\right]. \qquad (6)$$

Substituting Eq. (5) into Eq. (6), we find the expression for the limiting deformation:

$$|\epsilon_{22}| = \sqrt{3}\left[c_0 + \frac{\alpha}{3}(p_h - p_r)\right]\left(E_{2222}^*\left(1 - \frac{\alpha}{\sqrt{3}}\right)\right)^{-1}.$$

As a result, according to Eq. (6) the full limiting stress can written as follows:

$$|\sigma_{22}| = \sigma_{\text{st}} = \sqrt{3}\left[c_0 + \frac{\alpha}{3}(p_h - p_r)\right]\left(1 - \frac{\alpha}{\sqrt{3}}\right)^{-1} + (p_r - \Delta p_d). \qquad (7)$$

Note that while limiting stress σ_{st} obtained above does not depend on the proppant pack parameters except for the internal friction coefficient, the critical deformation $|\epsilon_{22}|$ depends on critical stress, bulk compression modulus, dilatancy coefficient and shear modulus of the pack.

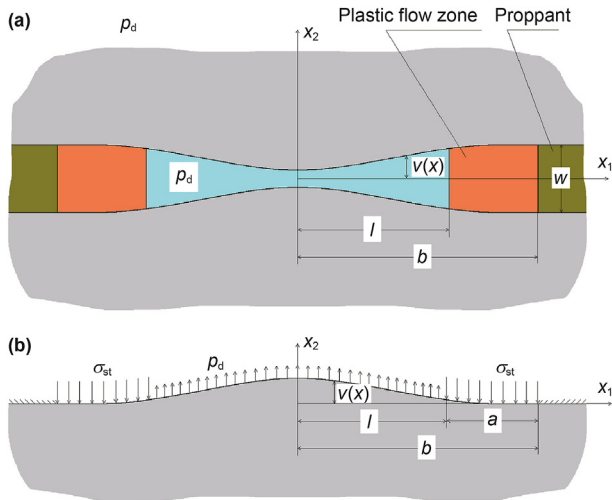We will now proceed with the study of the process of fracture

Fig. 5. Sketch of fracture deformation in the areas not supported by proppant (**a**) and the numerical scheme for calculation of closure of fracture faces (**b**).

Fig. 6. Near-wellbore proppant-free cavity in the fracture due to overflush or proppant flowback.

closure between the pillars within the plane strain approach (Fig. 5). On the free boundaries, the pressure $p_d = p_h - p_r + \Delta p_d$ is applied. In the zones of stress concentration, the tensile strength limit σ_{st} of the proppant pack (defined by Eq. (7)) is attained (Fig. 5a). To determine the displacements in this system, we will now consider the problem of a crack with a plastic zone $a = b - l$ in the tip area (Fig. 5b). This model can be used in our case under the assumption that there is plastic deformation in the proppant layer.

Displacements of the fracture faces v under the pressure drawdown Δp_d at $x_2 = 0$ and for the given distribution of loads takes the form Ishlinsky (1968):

$$\frac{v(x_1)}{l} = (1-v)\frac{p_d}{G}\sqrt{1 - \frac{x_1^2}{l^2}} \tag{9}$$

In order to determine the length of the plastic zone near the edge, we will use the solution of the Dugdale problem (Dugdale, 1960), which was obtained for the tensile crack with plastic zones. We will assume that plastic zone is formed as a result of the pressure drop Δp_d. In our case, the length of the plastic zone $a = b - l$ is determined by the relation:

$$\frac{l}{b} = \cos\left(\frac{\pi \Delta p_d}{2\sigma_{st}}\right), \tag{10}$$

$$v(x_1) = \frac{(1-v_s)}{\pi G_s}p_d\left\{2\left[\arcsin\frac{l}{b} - \frac{\sigma_{st}}{p_d}\left(\frac{\pi}{2} - \arcsin\frac{l}{b}\right)\right]\sqrt{b^2 - x_1^2} + \left[1 + \frac{\sigma_{st}}{p_d}\right][l\,v_1(x_1) - x_1\,v_2(x_1)]\right\},$$

$$v_1(x_1) = \ln\left|\frac{\sqrt{b^2 - x_1^2} + \sqrt{b^2 - l^2}}{\sqrt{b^2 - x_1^2} - \sqrt{b^2 - l^2}}\right|, \tag{8}$$

$$v_2(x_1) = \ln\left|\frac{l\sqrt{b^2 - x_1^2} + x_1\sqrt{b^2 - l^2}}{l\sqrt{b^2 - x_1^2} - x_1\sqrt{b^2 - l^2}}\right|.$$

Here, G_s and v_s are shear modulus and Poisson ratio of the matrix.

Neglecting the proppant deformation we find a simple formula for displacements:

where σ_{st} is the limiting stress determined by Eq. (7).

The walls of the fracture will close on the cavity under the condition that the maximum displacement of the fracture walls $v_{max} = v|_{x_1=0}$ is equal to the fracture half-width:

$$\frac{v_{max}}{l} = \frac{1-v}{\pi G}p_d\frac{b}{l}\left\{2\left(\arcsin\frac{l}{b} - \frac{\sigma_{st}}{p_d}\left(\frac{\pi}{2} - \arcsin\frac{l}{b}\right)\right) + \frac{l}{b}\left(1 + \frac{\sigma_{st}}{p_d}\right)\ln\left|\left(1 + \sqrt{1 - \left\{\frac{l}{b}\right\}^2}\right)\left(1 - \sqrt{1 - \left\{\frac{l}{b}\right\}^2}\right)^{-1}\right|\right\} \tag{11}$$
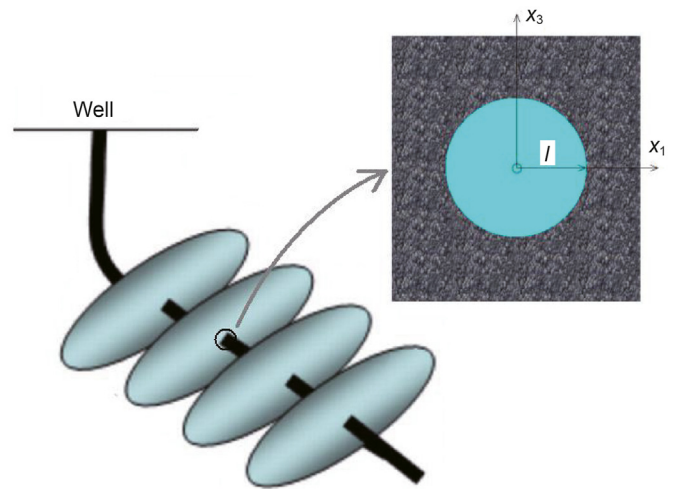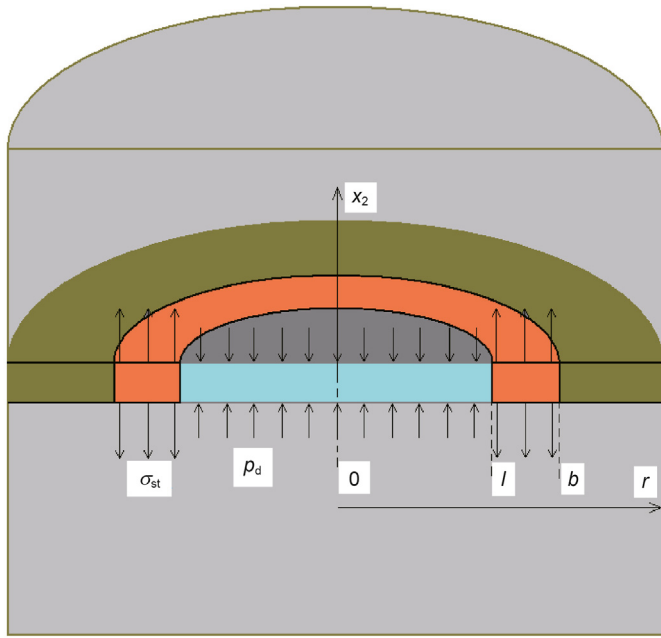
Fig. 7. Numerical scheme for the problem of fracture closure on the near-wellbore cavity.

As a result, one could find the maximum allowable pressure drawdown in the fracture Δp_d, which is within the safe operating interval in terms of the potential fracture pinchout between the proppant pillars.

2.1.2. Fracture closure in the near-wellbore zone

We will now consider the possibility for fracture closure in the near-wellbore zone. A proppant free zone may form within the fracture in the near-wellbore zone, because of an overflush during proppant placement (Osiptsov et al., 2018), or due to proppant flowback during aggressive well startup. Following the line of thought as we did in the case of fracture closure between proppant pillars, we formulate the problem using a radial axisymmetric configuration as shown in Fig. 6. Decrease of pressure in the fracture p_d results in the transition to plasticity of the proppant adjacent to the cavity (orange zone in Fig. 7).

The displacement of fracture faces can be written in the form (Sneddon, 1946):

$$v(r) = \frac{2(1-\nu)}{\pi G} \sqrt{b^2 - r^2} \left[\sigma_{st} \sqrt{1 - \frac{l^2}{b^2}} - p_d \left(1 - \sqrt{1 - \frac{l^2}{b^2}} \right) \right] \tag{12}$$

Assuming that the layer of proppant is strictly rigid (inelastic), i.e., $l = b$, we find the following formula for the displacement:

$$v(r) = \frac{2(1-\nu)}{\pi G} p_d \sqrt{b^2 - r^2}. \tag{13}$$

The length of the boundary of the plasticity zone can be determined by the formula (Li et al., 2013):

$$\frac{l}{b} = \sqrt{1 + 2\left(\frac{\Delta p_d}{\sigma_{st}}\right)} \left(\frac{\Delta p_d}{\sigma_{st}} + 1\right)^{-1}. \tag{14}$$

Thus we obtained above the solutions for fracture closure in both cases: between the proppant pillars in the bulk of the fracture and in the cavity near the wellbore (resulting from overflush or proppant flowback). Substituting Eq. (14) into Eq. (12), we obtain the following expression for the maximum displacement of the fracture face:

$$\frac{v_{max}}{l} = \frac{2(1-\nu)}{\pi G} \frac{\sigma_{st} + \Delta p_d}{\sqrt{\sigma_{st}^2 + 2\Delta p_d \sigma_{st}}} \left(\Delta p_d \frac{\sigma_{st} + p_d}{\sigma_{st} + \Delta p_d} - p_d \right). \tag{15}$$

2.1.3. Parametric study of fracture closure on proppant pillars

Consider the closure of a fracture between proppant pillars for a typical rock at the depth of $h = 3000$ m with the density of $\rho = 2500$ kg/m^3, Young modulus $E = 1.65 \times 10^{10}$ Pa and Poisson ratio $\nu = 0.25$. Cohesion of proppant particles $c_0 = 3.6 \times 10^4$ Pa and the inter-particle friction coefficient $\alpha = 0.707$. Pore pressure $p_r = 3.3 \times 10^7$ Pa, and the hydraulic fracturing pressure is calculated using the Eaton formula (Desroches and Bratton, 2000):

$$p_h = \frac{\nu}{1-\nu} (\sigma_{11}^0 - p_r) + p_r \tag{16}$$

In our case $p_h = 4.485 \times 10^7$ Pa. We will plot the graphs of relative displacement of fracture faces $v(x_1)/l$ for the pressure drop $\Delta p_d = 0.5 \times 10^7$ Pa (Fig. 8a), $\Delta p_d = 1.0 \times 10^7$ Pa (Fig. 8b). Red line shows displacements according to Eqs. (8) and (10) with account for deformable proppant. Dashed line corresponds to displacement in the case of absolutely rigid layer of proppant described by Eq. (9).
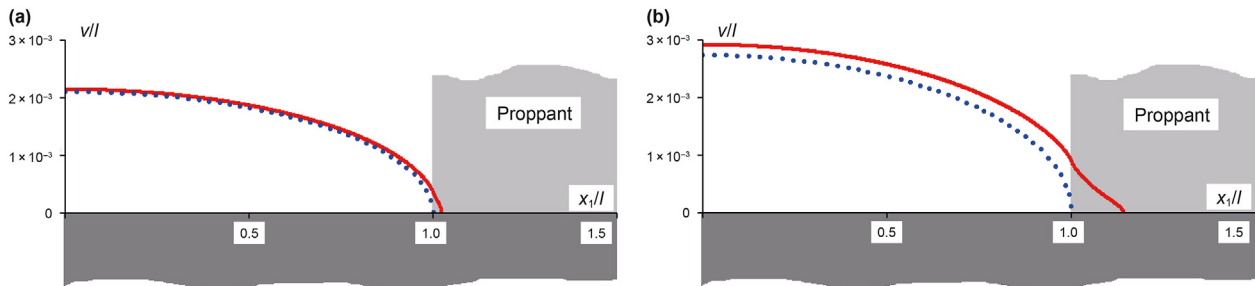

Fig. 8. Relative displacements of the fracture faces v_{max} between the pillars (plane problem) for the pressure drawdown of $\Delta p_d = 0.5 \times 10^7$ Pa (**a**) and $\Delta p_d = 1.0 \times 10^7$ Pa (**b**). Dashed line corresponds to the case of absolutely rigid proppant.
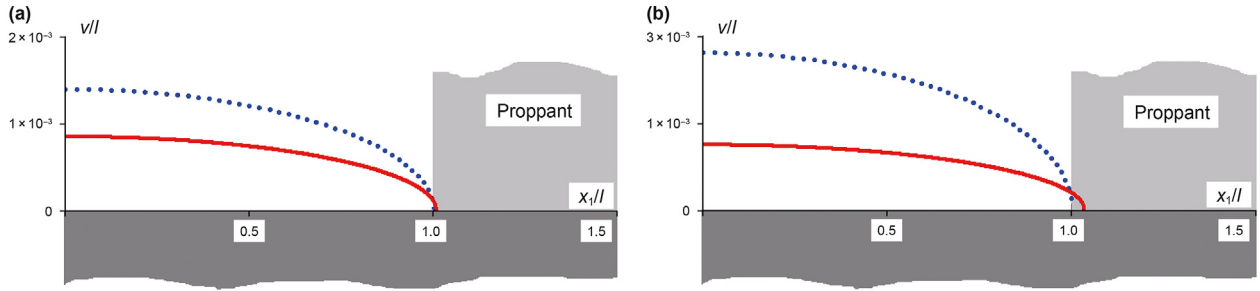
(a)

(b)

Fig. 9. Relative displacements of the fracture faces v_{max} near the wellbore (radial problem) for the pressure drawdown of $\Delta p_d = 0.5 \times 10^7$ Pa (**a**) and $\Delta p_d = 1.0 \times 10^7$ Pa (**b**). Red lines show displacements of the fracture face with account for proppant elasticity. Dashed line corresponds to the case of absolutely rigid proppant.
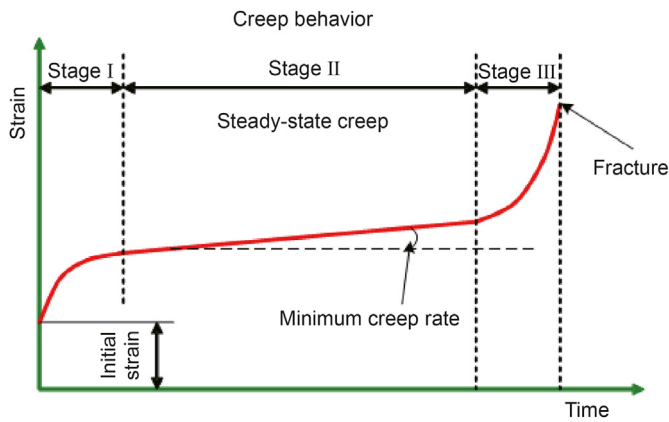

Fig. 10. A typical creep curve.

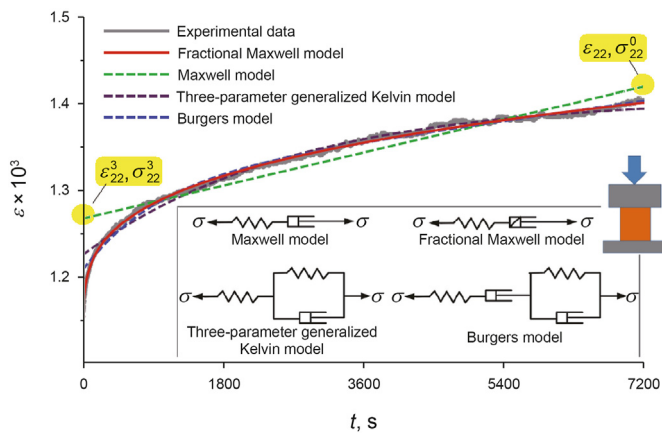**Fig. 11.** Maxwell model.

Fig. 12. Creep of tight sandstone from Changqing field. After Ding et al. (2017).

Comparison of the curves allows us to make conclusion that the account for proppant deformation leads to the increase in the amplitude of fracture faces bending.

A penny-shaped fracture behaves differently. According to Eqs. (12) and (14), in Fig. 9 we plotted red lines of relative displacement of the fracture faces $v(r)/l$ for the pressure drop $\Delta p_d = 0.5 \times 10^7$ Pa

(Fig. 8a) and $\Delta p_d = 1 \times 10^7$ Pa (Fig. 8b). Dashed line corresponds to displacements in the case of an absolutely rigid proppant (see Eq. (13)). It can be seen that, with pressure dropping, the displacements are smaller in the case of elastic proppant than in the case of absolutely rigid grains.

Comparison of Figs. 8 and 9 allows us to conclude that proppant elasticity plays differently in two cases: plane problem of fracture closure between the proppant pillars and radial problem of penny-shaped fracture closure near the wellbore. The reason is that there are two competing factors affecting the wall deformation. First one is an increase in fracture length with an increase in the plastic zone length which intensifies the displacements of fracture faces. The other one is that the stress in the plastic zone acts opposite to the pressure drawdown and thus mitigates the fracture wall displacements. In case of plane deformation, the former effect dominates as it is shown in Fig. 8. In the radial deformation problem, the latter effect is more significant due to larger plastic deformation area distributed along the circular zone as compared to that in the plane problem (see Fig. 9).

2.1.4. Fracture closure on proppant pillars in the presence of rock creep

Effect of the fracture closure may significantly amplify as a result of the rock creep. In Fig. 10, we demonstrate a typical curve of rock creep, which usually contains three intervals. The first interval is a transition to the long-term steady creep, which ends up with rock failure.

Frequently the Maxwell model of viscoelastic continuum is used to describe steady-state creep. The model effectively consists of two elements connected sequentially, a viscous one and an elastic one (Fig. 11). Constitutive relationship for the Maxwell model has a form:

$$\sigma + T_r \frac{d\sigma}{dt} = \eta \frac{d\epsilon}{dt}, \tag{17}$$

where T_r is the relaxation time, $T_r = \eta/E$.

The validity of the Maxwell model is confirmed, for example, in the study of creep in tight sandstones in the Changqing field (Ding et al., 2017) (Fig. 12). Using the creep curve shown in Fig. 12, we determine the parameters of the Maxwell model: $\eta = 2.25 \times 10^{14}$ Pa·s, $E = 3.937 \times 10^9$ Pa. Constitutive relationship of the Maxwell model can be represented as:

$$\sigma_{ij} = \frac{\hat{E}}{1+\nu} \left(\epsilon_{ij} + \frac{\nu}{1-2\nu} \epsilon \delta_{ij} \right), \tag{18}$$
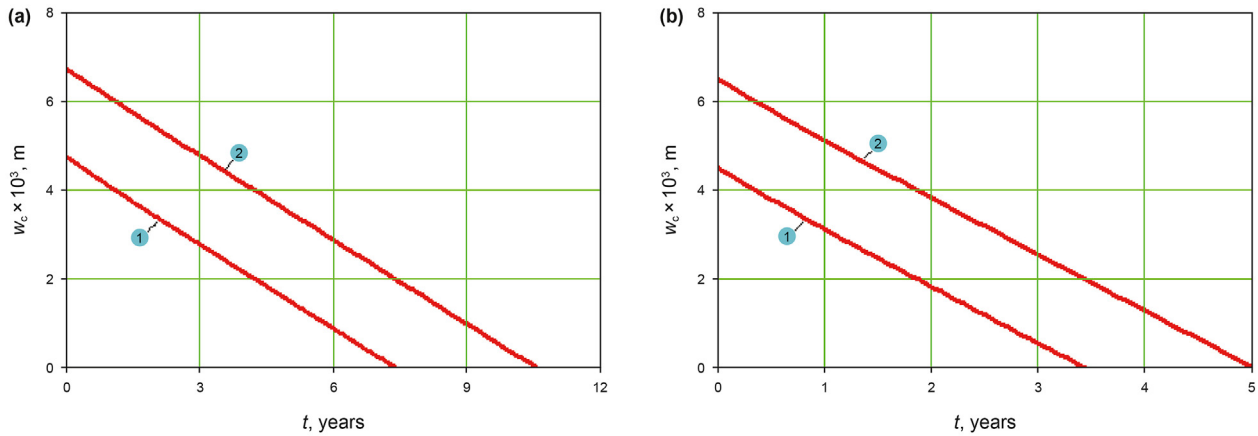
with

Fig. 13. Fracture closure w_c with time t in the near-wellbore zone for the proppant-free cavity radius $l = 0.125$ m (**a**) and $l = 0.25$ m (**b**) and the initial fracture opening $w_0 = 5 \times 10^{-3}$ m (curve 1) and $w_0 = 7 \times 10^{-3}$ m (curve 2).

$$\hat{E} = \frac{\eta D}{1 + T_r D}, \quad D = \frac{d}{dt}.$$

Using Eq. (18), we transform the solutions obtained above into the solutions for the visco-elastic medium. Thus, for example the velocity of fracture faces closure near the wellbore (Fig. 7) can be written as, according to Eq. (13):

$$\frac{d\nu_{max}/l}{dt} = \frac{4(1 - \nu^2)}{\pi\eta}\left(A_p + T_r\frac{dA_p}{dt}\right), \tag{19}$$

where

$$A_p = p_d\frac{\sigma_{st} + \Delta p_d}{\sqrt{\sigma_{st}^2 + 2\Delta p_d\sigma_{st}}}\left(\frac{\Delta p_d}{p_d}\frac{\sigma_{st} + p_d}{\sigma_{st} + \Delta p_d} - 1\right). \tag{20}$$

For the creep of fracture faces between proppant pillars, based on Eqs. (18) and (11), we write:

$$\frac{d\nu_{max}/l}{dt} = \frac{2(1 - \nu^2)}{\pi\eta}\left(A + T_r\frac{dA}{dt}\right), \tag{21}$$

where

$$A_p = p_d\left(2 - \cos\left(\frac{\pi p_d}{2\sigma_{st}}\right)\right)\left[2\left[\arcsin\frac{l}{b} - \frac{\sigma_{st}}{p_d}\left(\frac{\pi}{2} - \arcsin\frac{l}{b}\right)\right] + \frac{l}{b}\left(1 + \frac{\sigma_{st}}{p_d}\right)\ln\frac{\left(1 + \sqrt{1 - (l/b)^2}\right)}{\left(1 - \sqrt{1 - (l/b)^2}\right)}\right].$$
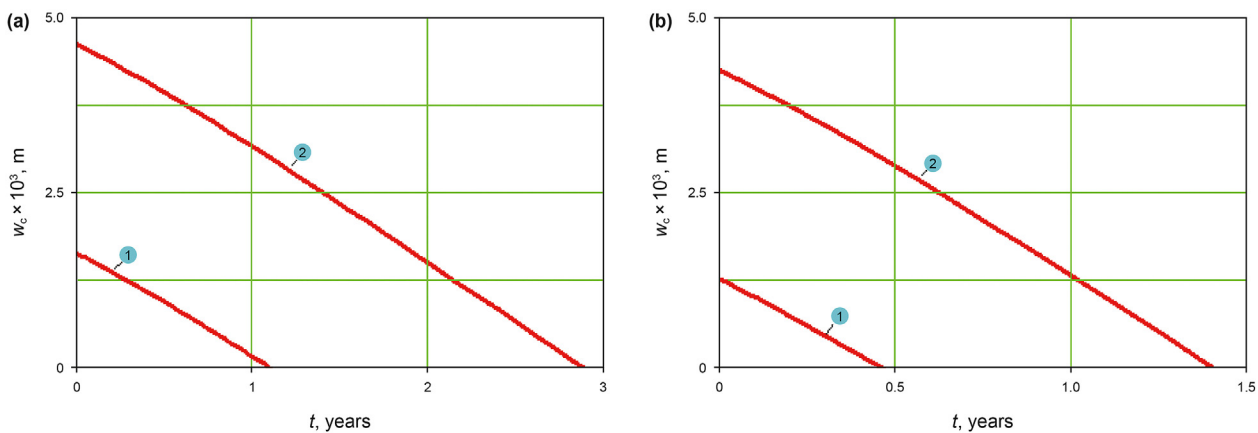

Fig. 14. Fracture closure w_c with time t between proppant pillars for the inter-pillar distance $l = 0.125$ m (**a**) and $l = 0.25$ m (**b**) and the initial fracture opening $w_0 = 2 \times 10^{-3}$ m (curve 1) and $w_0 = 5 \times 10^{-3}$ m (curve 2).

2.1.5. Parametric study of fracture closure on proppant pillars in the presence of rock creep

For a particular calculation of the rock creep, let us assume the following values of the governing parameters: $\eta = 2 \times 10^{17}$ Pa·s, Young modulus $E = 1.65 \times 10^{10}$ Pa, Poisson ratio $\nu = 0.22$, and the relaxation time $T_r = 1.333 \times 10^7$ s, $p_r = 3.3 \times 10^7$ Pa.

Calculations according to Eq. (19) allow us to analyze the process of fracture closure $w = w_0 - 2v_{max}(t)$ in the near-wellbore area. In simulations, the pressure decline was assumed exponential $\Delta p_d = \Delta p_{max}[1 - \exp(kt)]$ for $k = 4.4 \times 10^{-8}$ s^{-1}, which corresponds to pressure decline by the magnitude of Δp_{max} during the period of two years. Calculations are carried out for $\Delta p_{max} = 1.0 \times 10^7$ Pa and initial radius of $l = 0.125$ m. For the initial opening of $w_0 = 5 \times 10^{-3}$ m, we have shown that fracture closure and pinch-out in the near-wellbore zone occurs within about 7 years (Fig. 13a, curve 1). For the initial opening of $w_0 = 7 \times 10^{-3}$ m, the time of fracture closure increases up to 10 years. In the case of larger initial radius $l = 0.25$ m, the closure develops faster: for $w_0 = 5 \times 10^{-3}$ m it takes 3 years, and for $w_0 = 7 \times 10^{-3}$ m − 5 years (Fig. 13b).

Consider now fracture closure between proppant pillars (which are formed as a result of alternate slug fracturing). Using Eq. (21), we evaluate the process of fracture closure between pillars for the distance of $l = 0.125$ m (Fig. 14a) and $l = 0.25$ m (Fig. 14b) for the initial fracture opening of $w_0 = 2 \times 10^{-3}$ m (curve 1) and $w_0 = 5 \times 10^{-3}$ m (curve 2).

We note that, with the increase in the spacing between proppant pillars from 0.125 m to 0.25 m, the time taken for fracture closure and pinch-out drops by a factor of three. Comparison of Figs. 13 and 14 shows that fracture closure between pillars (plane problem) is more pronounced than it is in the near-wellbore zone (axisymmetric problem). The same conclusion is valid for the comparison of plastic zones. Rapid fracture pinch out between the proppant pillars is related to relatively small fracture opening as well as to the plane character of the problem of fracture closure (see Fig. 2). For the same load, plane system (fracture opening between pillars) shows larger deformations (more pronounced fracture closure) as compared to the axisymmetric problem (near-wellbore fracture zone, Fig. 6).

2.2. Variation of stress state in the vicinity of a fracture during flowback and production

During pressure decrease in a fracture, a stretching force Δp_s is exerted on the fracture face (Fig. 15a). Associated increase in the shear stress may lead to the transition of the material to plasticity at the fracture face. Fluid filtration into the fracture will gradually change effective stresses in the adjacent domains, which will lead to formation of plasticity zone and its expansion into the ambient rock (Fig. 15b).
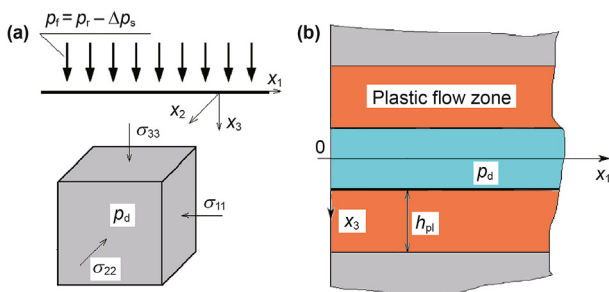

Fig. 15. Hydraulic fracture and formation of plasticity zones.

2.2.1. Problem formulation

To study the expansion of plasticity zone into the rock surrounding the fracture, we will formulate the mass balance equation for elastoplastic medium in 1D using the key constitutive relationships of the Biot poroelasticity model and constitutive relationships of an elastoplastic medium with internal friction. Heterogeneity of pore pressure field p creates filtration fluxes, which can be expressed via Darcy law:

$$q_i^m = -\frac{k_r}{\mu}\frac{\partial p}{\partial x_i}, \tag{22}$$

where q_i^m is the mass transfer rate through a unity square in a time unit in the i-th direction, k_r is rock permeability, and μ is fluid viscosity.

Variation in fluid content in the unit volume of a porous medium ζ is related to the bulk deformation of the porous medium $\epsilon = \epsilon_{11} + \epsilon_{22} + \epsilon_{33}$ by the formula (see Detournay and Cheng, 1993):

$$p = M(\zeta - \beta\epsilon), \tag{23}$$

with

$$\beta = 1 - \frac{K}{K_s}, \quad M = \frac{K_f}{\varphi_r + (\beta - \varphi_r)(1 - \beta)K_f / K}. \tag{24}$$

where β is the Biot coefficient; and M is the Biot module; K is bulk modulus of the fluid-saturated medium in drainage conditions; K_s is the bulk modulus of the rock matrix and φ_r is rock porosity.

In view of Eqs. (22) and (23), the mass balance equation

$$\frac{\partial \zeta}{\partial t} = -q_{i,j}$$

takes the form

$$\frac{1}{M}\frac{\partial p}{\partial t} = \frac{k}{\mu}\nabla^2 p - \beta\frac{\partial \epsilon}{\partial t}. \tag{25}$$

In order to find bulk deformation ϵ, Eq. (25) should be complemented with the balance condition:

$$\frac{\partial \sigma_{ij}}{\partial x_j} = 0 \tag{26}$$

and the Prandtl-Reuss constitutive relationships for the components of the stress increments tensor $d\sigma_{ij}$ and the components of the strain increments tensor $d\epsilon_{kl}$,

$$d\sigma_{ij}^{eff} = E_{ijkl}d\epsilon_{kl}, \tag{27}$$

where $\sigma_{ij}^{eff} = \sigma_{ij} + p\delta_{ij}$.

Coefficients of constitutive relationships determined by Eq. (27) are described by Eq. (2) with dilatancy Λ set to zero (Rudnicki and Rice, 1975).

According to Eq. (2), plastic flow is determined by the deviatoric part of the stress tensor $s_{ij} = \sigma_{ij}^{eff} - \delta_{ij}\sigma_{eff}$, mean stress $\sigma_{eff} = \sigma_{ij}^{eff}/3$ and intensity of shear stress

$$T = \sqrt{\frac{1}{2}s_{ij}s_{ij}}. \tag{28}$$

We consider the case of 1D filtration corresponding to linear filtration regime in reservoir and assume that $\epsilon_{11} = \epsilon_{22} = 0$ and $\epsilon = \epsilon_{33}$. In this case, Eq. (27) take the form:

$$\mathrm{d}(\sigma_{11} + \beta p) = E_{1133}\mathrm{d}\epsilon_{33}, \quad \mathrm{d}(\sigma_{22} + \beta p) = E_{2233}\mathrm{d}\epsilon_{33},$$
$$\mathrm{d}(\sigma_{33} + \beta p) = E_{3333}\mathrm{d}\epsilon_{33}. \tag{29}$$

Assuming that $\sigma_{22}^{\mathrm{eff}} = \sigma_{11}^{\mathrm{eff}}$ and taking into account expressions for the deviatoric part of the stress tensor

$$s_{11} = s_{22} = \frac{1}{3}(\sigma_{11}^{\mathrm{eff}} - \sigma_{33}^{\mathrm{eff}}), \quad s_{33} = -\frac{2}{3}(\sigma_{11}^{\mathrm{eff}} - \sigma_{33}^{\mathrm{eff}}),$$

we rewrite the intensity of shear stress defined by Eq. (28) in the form

$$T = \frac{1}{\sqrt{3}}\left|\sigma_{33}^{\mathrm{eff}} - \sigma_{11}^{\mathrm{eff}}\right|$$

As a result, elastic moduli can be written as

$$E_{1133} = E_{2233} = K - \frac{2}{3}G + A_{\mathrm{c}}$$

$$E_{3333} = K + \frac{4}{3}G + 2A_{\mathrm{c}}$$

$$A_{\mathrm{c}} = \mathrm{sgn}\left(\sigma_{11}^{\mathrm{eff}} - \sigma_{33}^{\mathrm{eff}}\right)\frac{1}{\sqrt{3}}\frac{G^2}{H+G} \times \left(-\mathrm{sgn}\left(\sigma_{11}^{\mathrm{eff}} - \sigma_{33}^{\mathrm{eff}}\right)\frac{2}{\sqrt{3}} + \frac{K}{G}\alpha\right)$$

Substituting Eq. (29) into the balance equation (Eq. (26)), we obtain:

$$\epsilon = \epsilon_{33} = E_{3333}^{-1}\beta p, \tag{30}$$

According to Eq. (30), the mass balance equation (Eq. (25)) takes the form:

$$\frac{\partial p}{\partial t} - \kappa\frac{\partial^2 p}{\partial x_3^2} = 0, \tag{31}$$

with

$$\kappa = \frac{k}{\mu}\left(\beta^2 E_{3333}^{-1} + \frac{1}{M}\right)^{-1}$$

We will now determine the condition at the boundary of the plastic flow zone, using the Drucker-Prager threshold condition:

$$T + \alpha\sigma^{\mathrm{eff}} = c \tag{32}$$

with

$$T = \frac{1}{\sqrt{6}}\sqrt{(\sigma_{11}^{\mathrm{eff}} - \sigma_{22}^{\mathrm{eff}})^2 + (\sigma_{22}^{\mathrm{eff}} - \sigma_{33}^{\mathrm{eff}})^2 + (\sigma_{33}^{\mathrm{eff}} - \sigma_{11}^{\mathrm{eff}})^2},$$

where $\sigma^{\mathrm{eff}} = \sigma_{ij}^{\mathrm{eff}}\delta_{ij}$ is the mean stress; c is cohesion; $\alpha = \sin\varphi_{\mathrm{a}}$ is the internal friction coefficient, and φ_{a} is the internal friction angle.

Stresses at the boundary of the fracture wall are determined from the relations

$$\sigma_{33}^{\mathrm{eff}} = p(1 - \beta), \quad \lambda = \frac{\nu}{1 - \nu}$$
$$\sigma_{11}^{\mathrm{eff}} = \sigma_{11}^{0(\mathrm{eff})} - \beta p - \lambda p(1 - \beta), \tag{33}$$
$$\sigma_{22}^{\mathrm{eff}} = \sigma_{22}^{0(\mathrm{eff})} - \beta p - \lambda p(1 - \beta),$$

where $\sigma_{11}^{0(\mathrm{eff})}, \sigma_{22}^{0(\mathrm{eff})}$ are the initial stresses caused by the overburden weight.

Initial stress $\sigma_{22}^{0(\mathrm{eff})}$ depends on the weight of the rock as well as on tectonic stress $\sigma_{22}^{\mathrm{t(eff)}}$ and is equal to $\sigma_{22}^{0(\mathrm{eff})} = \lambda\sigma_{11}^{0(\mathrm{eff})} + \sigma_{22}^{\mathrm{t(eff)}}$. Substituting Eq. (33) into Eq. (32), we find the expression of the pressure p_{pl} at the boundary of the plasticity zone h_{pl}. The corresponding equation is non-linear and can be solved, for example, by the Newton method. In case when the rock stress are equal $\sigma_{11}^{0(\mathrm{eff})} = \sigma_{22}^{0(\mathrm{eff})}$, the expression for p_{pl} is as follows:

$$p_{\mathrm{pl}} = \left(c\sqrt{3} + \sigma_{11}^{0(\mathrm{eff})}\left(1 - \frac{2\alpha}{\sqrt{3}}\right)\right)\left((1 - \lambda)(1 - \beta) + \beta + \frac{\alpha}{\sqrt{3}}\left[-2\beta + (1 + 2\lambda)(1 - \beta)\right]\right)^{-1} \tag{34}$$

Now let us formulate the problem of the motion of the front of plastic flow. Assume that, at the initial time instant, pore pressure in the matrix is overall uniform and equal to p_{r}. Then, pressure in the fracture at the boundary $x_3 \geq 0$ at $t = 0$ decreases to the value of p_{f} and in what follows is maintained the same (Fig. 15). In distanced points at $x_3 \to \infty$, the pressure remains constant and is equal to p_{r}. Assume that stresses in the domain $0 \leq x_3 \leq x_3^{(1)}(t)$ exceed the strength limit (Fig. 16). The pressure within this domain is denoted as $p^{(1)}$ and outside this domain as $p^{(2)}$, we write the mass balance equations:

$$\frac{\partial p^{(2)}}{\partial t} - \kappa^{(2)}\frac{\partial^2 p^{(2)}}{\partial x_3^2} = 0, \quad x_3^{(1)} \leq x_3 \leq \infty$$
$$\frac{\partial p^{(1)}}{\partial t} - \kappa^{(1)}\frac{\partial^2 p^{(1)}}{\partial x_3^2} = 0, \quad 0 \leq x_3 \leq x_3^{(1)} \tag{35}$$
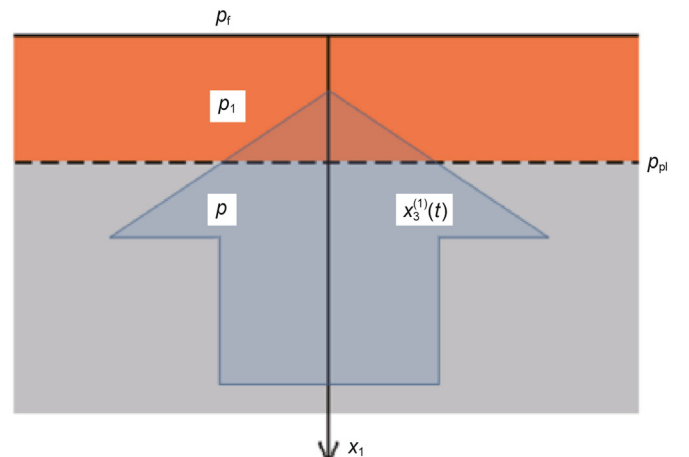
with

Fig. 16. Propagation front of the plasticity zone.

$$\kappa^{(2)} = M \frac{k}{\mu}\left(1 + \beta^2 \frac{M}{2G}\frac{1-2\nu}{1-\nu}\right)^{-1},$$

$$\kappa^{(1)} = M \frac{k}{\mu}\left(1 + \beta^2 M E_{3333}^{-1}\right)^{-1}.$$

Corresponding boundary and initial conditions take the form:

$$
\begin{aligned}
x_3 = 0, \quad t > 0: \quad & p(x_3, t) = p \\
x_3 = \infty, \quad t \geq 0: \quad & p(x_3, t) = 0 \\
t = 0: \quad & p(x_3, t) = 0
\end{aligned}
\tag{36}
$$

These conditions are complemented by the equality of pressure at the boundary between the plastic and elastic domains:

$$x_3 = x_3^{(1)}: \quad p^{(2)}(x_3^{(1)}, t) = p_1(x_3^{(1)}, t) = p_{\mathrm{pl}} = \mathrm{const}.$$

Note that this formulation is equivalent to the Stefan problem of propagation of a solidification front (see Gupta (2017); Osiptsov (2007)). Since the front is moving with an a priori unknown velocity, there must be an additional condition specified at this front, in addition to boundary and initial conditions Eq. (36) for equations Eq. (35). Let the front be displaced at a distance $\mathrm{d}x_3^{(1)}$ over the time $\mathrm{d}t$. In this case, the volume of fluid on the left and on the right of the front should be equal to the volume of the pores in the area overcome by the front over $\mathrm{d}t$. When approaching the boundary from the plastic zone, the porosity adjusted for deformation and determined according to Eq. (30) is equal to

$$\varphi_{\mathrm{pl}} = \varphi_{\mathrm{r}} + E_{3333}^{-1}\beta p_{\mathrm{pl}},$$

and the limit when approaching the front from the elastic zone is:

$$\varphi_{\mathrm{e}} = \varphi_{\mathrm{r}} + \left(K + \frac{4}{3}G\right)^{-1}\beta p_{\mathrm{pl}},$$

As a result, using the Darcy law determined by Eq. (22) we obtain the equation:

$$x_3 = x_3^{(1)}(t): \quad \frac{k}{\mu}\frac{\partial p_1}{\partial x_3} - \frac{k}{\mu}\frac{\partial p^{(2)}}{\partial x_3} = -\Delta\varphi\frac{\partial x_3^{(1)}}{\partial t}$$

with

$$\Delta\varphi = \varphi_{\mathrm{pl}} - \varphi_{\mathrm{el}} = \left[E_{3333}^{-1} - \left(K + \frac{4}{3}G\right)^{-1}\right]\beta p_{\mathrm{pl}}.$$

Solution of Eq. (35) with conditions formulated above in Eq. (36) leads to the following distribution of pressure (details of the derivation are given in Appendix 3):

$$0 \leq x_3 \leq x_3^{(1)}:$$

$$p^{(1)} = p^{(2)} + (p_{\mathrm{pl}} - p^{(2)})\mathrm{erf}\left(\frac{x_3}{2\sqrt{\kappa^{(1)}t}}\right)\left[\mathrm{erf}\left(\frac{\chi}{2\sqrt{\kappa^{(1)}}}\right)\right]^{-1}$$

$$\tag{37}$$

$$x_3^{(1)} \leq x_3 \leq \infty:$$

$$p^{(2)} = p_{\mathrm{pl}}\left(1 - \mathrm{erf}\left(\frac{x_3}{2\sqrt{\kappa^{(2)}t}}\right)\right)\left[1 - \mathrm{erf}\left(\frac{\chi}{2\sqrt{\kappa^{(2)}}}\right)\right]^{-1}$$

The front of plasticity $x_3 = x_3^{(1)}$ is moving with the following velocity v_{pl} expressed as follows:

$$v_{\mathrm{pl}} = \frac{\partial x_3^{(1)}}{\partial t} = \frac{\chi}{2\sqrt{t}}\tag{38}$$

In order to use the relations obtained above in simulations, one needs to evaluate the Biot parameters β and M (see Eq. (24)) and, consequently, elastic properties of the rock matrix E_{s} and ν_{s}. To determine matrix properties, we consider relations of the mechanics of media with a large number of pores and fractures Kachanov et al. (1994):

$$
\begin{aligned}
\frac{E}{E_{\mathrm{s}}} &= \left[1 + \frac{\varphi_{\mathrm{r}}}{1-\varphi_{\mathrm{r}}}\frac{3(1-\nu_{\mathrm{s}})(9+5\nu_{\mathrm{s}})}{2(7-5\nu_{\mathrm{s}})}\right]^{-1}, \\
\nu &= \frac{E}{E_{\mathrm{s}}}\left[\nu_{\mathrm{s}} + \frac{\varphi_{\mathrm{r}}}{1-\varphi_{\mathrm{r}}}\frac{3(1-\nu_{\mathrm{s}})(9+5\nu_{\mathrm{s}})}{2(7-5\nu_{\mathrm{s}})}\right].
\end{aligned}
\tag{39}
$$

Here, E and ν are corresponding effective mechanical parameters of fluid-saturated rock.

Using Eq. (39), we find Poisson ratio for the rock material:

$$\nu_{\mathrm{s}} = \frac{B - \sqrt{B^2 - 4AC}}{2A},$$

with

$$A = 5\left[3\frac{\varphi_{\mathrm{r}}}{1-\varphi_{\mathrm{r}}}(1-\nu) + 2\right],$$

$$B = 2\left[6\frac{\varphi_{\mathrm{r}}}{1-\varphi_{\mathrm{r}}}(1+\nu) + 5\nu + 7\right],$$

$$C = \left[3\frac{\varphi_{\mathrm{r}}}{1-\varphi_{\mathrm{r}}}(9\nu - 1) + 14\nu\right].$$

2.2.2. Parametric study of plastic zone propagation in rock formation surrounding hydraulic fracture during flowback

Assume the following particular values of the governing parameters: fluid viscosity $\mu = 10^{-3}$ Pa·s, rock permeability $k = 0.986 \times 10^{-15}$ m^2 (1 mD), fluid bulk modulus $K_{\mathrm{f}} = 2\times 10^9$ Pa, porosity $\varphi_{\mathrm{r}} = 0.17$, Young modulus $E = 1.65 \times 10^{10}$ Pa, Poisson ratio $\nu = 0.25$, cohesion $c = 5.87 \times 10^6$ Pa, and internal friction coefficient $\alpha = 0.86$.

Based on Eqs. (38 and 39), we determine the rock parameters $E_{\mathrm{s}} = 2.328 \times 10^{10}$ Pa, $\nu_{\mathrm{s}} = 0.261$, and then the Biot parameters: $\beta = 0.322$ and $M = 1.06 \times 10^{10}$ Pa.

Assuming the rock density of $\rho = 2500$ kg/m^3, we find initial stresses at the depth of $h = 3000$ m. Specifying pore pressure of $p_{\mathrm{r}} = 3.3 \times 10^7$ Pa, we use Eq. (34) to calculate the pressure drop at which the tensile strength is exceeded: $p_{\mathrm{pl}} = 9.73 \times 10^6$ Pa. Then, specifying the pressure drop to be $p = 1.2 \times p_{\mathrm{pl}}$ and solving Eq. (71), we obtain the parameters $\Delta\varphi = 4.1 \times 10^{-2}$ and $\chi = 0.31$. This allows us to plot the propagation velocity of the plasticity front v_{pl} (Fig. 17a) according to Eq. (38) and its coordinate $x_3^{(1)}$ (Fig. 17b) as functions of time.

For porosity of $\varphi_{\mathrm{r}} = 0.04$ we obtain $p_{\mathrm{pl}} = 7.23 \times 10^6$ Pa, $\Delta\varphi = 8.1 \times 10^{-3}$, $\chi = 0.063$, and the Biot parameters: $\beta = 0.0862$ and 4.195×10^{10} Pa. Note that the smaller the porosity, the faster is the propagation of the plasticity front (i.e., in the case of a more monolithic material).

The equation constructed above allows one to obtain the Carter leak-off coefficient C_{L} with the help of analytical solution determined by Eq. (37) and Darcy law (see Eq. (22)). As a result, we find the rate of mass transfer through the boundary $x_3 = 0$:
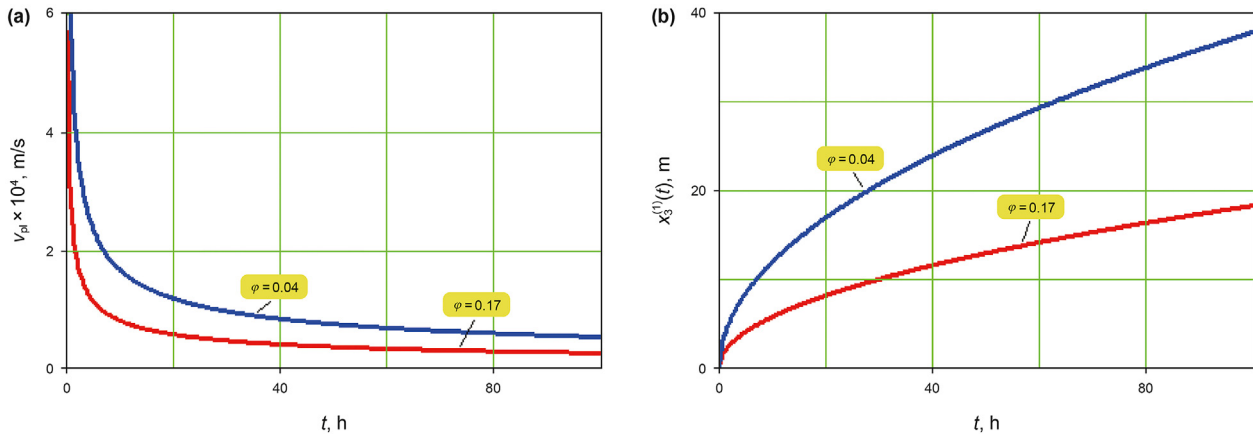
Fig. 17. Propagation velocity of the plasticity front v_{pl} (**a**) and its coordinate $x_3^{(1)}$ (**b**) as functions of time (in hours).

$$q|_{x_3=0} = \frac{C_L}{\sqrt{t}}, \tag{40}$$

with

$$C_L = \frac{p^{(2)} - p_{pl}}{\sqrt{\pi \kappa^{(1)}} \, \text{erf}(\chi / 2\sqrt{\kappa^{(1)}})} \tag{41}$$

At the end of this section we would like to note that the proposed solution, while based on well-known theoretical approaches of mechanics of deformable media, contains a number of simplifying assumptions related to evolution of pore pressure and fluid filtration in the rock formation surrounding hydraulic fracture as well as to rock deformation process. Validation of the proposed model can be carried out in a thoroughly-planned laboratory experiment, which is out of the scope of our study.

3. Impact of fluid-fluid displacement on fracture conductivity

In the current section we formulate the mathematical model of filtration in a propped fracture during flowback with account of geomechanics (non-elastic proppant pack compaction, proppant embedment, tensile rock failure and fracture closure in between proppant pillars) and fluid mechanics effects (multiphase filtration, fines transport, proppant pack colmatation and displacement of yield-stress fracturing fluid representing unbroken cross-linked gel). Our goal is to study the fracture conductivity and cleanup dynamics during flowback, and, in particular, to investigate the relative importance of various factors contributing to fracture conductivity degradation.

We assume that during flowback the hydraulic fracture is closed on proppant pack (either uniform or in isolated pillars), which is filled initially with the yield-stress fracturing fluid (unbroken cross-linked gel). While accurate study of flowback in a fracture filled heterogeneously with proppant pillars requires 2D formulation, we study it in a simplified 1D formulation. This allows to analyze quantitatively the effect of fracture closure in between isolated proppant pillars in typical flowback conditions.

Before the start of flowback, the pore pressure inside the proppant pack is equal to the pore pressure inside the surrounding rock matrix, so that the "fracture-rock" system is in equilibrium. Then the bottom-hole pressure in the well decreases according to a certain dynamics of the choke opening at the surface, which triggers the influx of reservoir fluid through the fracture walls. At this

stage, surface choke dynamics is represented by a piece-wise constant bottom-hole pressure as a function of time, while in our future studies, we plan to develop a coupled "wellbore-hydraulic fracture" model.

For simplicity, we consider the flowback in a single wing of a hydraulic fracture approximated by a 1D model, which assumes that the fracture is elongated in the horizontal direction, its height is constant, while its aperture is a function of coordinate and time according to geomechanics model describing fracture compaction and proppant embedment. Details of the mathematical model of fracture flowback are presented below.

3.1. 1D model for fluid-fluid displacement in a fracture

Fracture flowback model including various hydrodynamical and geomechanical effects was formulated in our previous study (Osiptsov et al., 2020). The model takes into account proppant embedment and compaction (which are inelastic processes), as well as compressibility of fluids and transport of solid particles. In the current study we extend the model by taking into account the following effects: (i) viscoplastic rheology of hydraulic fracturing fluid, which mimics the unbroken cross-linked gel filling initially the proppant pack due to failure of breakers (Al-Fariss and Pinder, 1987; Bird, 2002), and (ii) coupled model for influx from reservoir taking into account two-phase filtration in reservoir in linear regime, while in our previous study we used Carter law for reservoir-fracture flux based on analytical solution to pressure diffusion equation in reservoir valid for single-phase filtration and uniform initial pore pressure distribution (Carter, 1957).

Governing equations describing fracture flowback are formulated as follows:

$$\frac{\partial}{\partial t}[\rho_i^f s_i \varphi w] + \frac{\partial}{\partial x}(\rho_i^f u_i w) = \rho_i q_i, \ \ i = 1, 2; \tag{42}$$

$$u_1 = -\frac{\nabla p}{|\nabla(p)|}\left[\frac{kk_1}{\mu_1}(|\nabla p| - \alpha_y \tau_y)\right]^{1/n}, \quad |\nabla p| - \alpha_y \tau_y > 0, \tag{43}$$

$$u_1 = 0, \ \ |\nabla p| - \alpha_y \tau_y \leq 0, \ \ \alpha_y = \sqrt{\frac{\varphi C'}{2k}}, \tag{44}$$

$$\mu_1 = \frac{H_f}{4}\left(3 + \frac{1}{n}\right)^n (8k\varphi C')^{(1-n)/2} \tag{45}$$

$$u_2 = -\frac{kk_2}{\mu_2}\nabla p, \tag{46}$$

$$k = \frac{r_p^2\varphi^3}{C'(1-\varphi)^2}, \tag{47}$$

$$w = w_0(1-\epsilon_{33}) - 2e_0, \tag{48}$$

$$\varphi = \varphi_0 - \epsilon_{33}, \tag{49}$$

$$\rho_i^f(p) = \rho_{i,0}^f(1.0 + \beta_i[p - p_0]) \tag{50}$$

Here by index $i = 1, 2$ we denote parameters of hydraulic fracturing fluid and oil, respectively; $\rho_i^f(p)$ are densities of the fluids (β_i are fluid compressibilities and $\rho_{i,0}^f$ are fluid densities at the reference pressure p_0); s_i are fluid saturations inside the proppant pack; φ and φ_0 are current and initial porosities of the pack; w and w_0 are current and initial apertures of the fracture; u_i are filtration velocities of the fluids, q_i are fluid filtration velocities at the fracture walls describing influx from reservoir (we neglect the volume of fluid leaked off into formation during hydraulic fracturing process, so that $q_1 = 0$); k is permeability of the pack; r_p is the proppant radius, k_i are relative permeabilities of proppant pack; μ_1 is effective viscosity of the hydraulic fracturing fluid (plastic viscosity) described by Herschel-Bulkley rheology model with consistency index H_f, power-law index n and yield stress τ_y; μ_2 is oil viscosity; p is fluid pressure inside the proppant pack, x is the coordinate along fracture, ϵ_{33} is relative deformation of proppant pack due to compaction, e_0 is the depth of embedment into fracture walls, C' is a constant in Cozeny-Carman correlation between proppant pack porosity, permeability and particle diameter. Eq. (47) describes the relation between the permeability and porosity of the proppant pack (Carman, 1937). More details on models describing proppant pack compaction and embedment models are provided in Appendix 1.

In numerical implementation of the fracture flowback model described above we use alternative and equivalent form of Eqs. (43) and (45) (originally formulated in (Al-Fariss and Pinder, 1987; Bird, 2002)) describing filtration of yield-stress fluid and effective viscosity:

$$u_1 = -\frac{kk_1}{\mu_1}g(|\nabla(p)|)\nabla p, \quad |\nabla p| - \alpha\tau_y > 0, \tag{51}$$

$$g(|\nabla(p)|) = \left(1 - \frac{\alpha\tau_y}{|\nabla(p)|}\right)^{1/n}, \quad |\nabla(p)| = \left|\frac{\partial p}{\partial x}\right| \tag{52}$$

$$\mu_1 = |\nabla(p)|^{(n-1)/n}\frac{3n+1}{2n}\left(\frac{\sqrt{2}}{2}\right)^{(n+1)/n}\left(\frac{\varphi C'}{k}\right)^{(1-n)/(2n)}H_f^{1/n} \tag{53}$$

Here, function $g(|\nabla(p)|)$ varies in the range in between 0 and 1 and describes a decrease in mobility of a yield-stress fluid when local pressure gradient approaches the critical value $\alpha\tau_y$; note that effective viscosity determined by Eq. (53) differ from that described by Eq. (45).

The difference of current filtration model from the previous one, presented in Osiptsov et al. (2020), is taking into account visco-plastic rheology of fractured fluid as described by Eqs. (43)–(45) obtained in Al-Fariss and Pinder (1987) for filtration of fluid with Hershel-Bulkley rheology (in the simulations we consider Bingham rheology with $n = 1$).

Filtration model described by Eqs. (42), (46), (50) and (51) (with $w = 1$ and $q_i = 0$) is also used to describe filtration of Newtonian fluids (water and oil) in the reservoir, in contrast with the model described in Osiptsov et al. (2020), where flux from a rock formation into the fracture is described using Carter law. Note that Carter analytical solution to pressure diffusion equation is valid only for single-phase filtration, uniform initial pressure distribution in reservoir and steady pressure in the fracture. The model determined by Eqs. (42), (46), (50) and (51) allows considering multiphase filtration, transient pressure in hydraulic fracture and initial non-uniform pressure distribution is the rock formation after hydraulic fracturing. We assume that only water phase from fracturing fluid penetrate into the reservoir, so that leaked-off fracturing fluid is water (with similar parameters as that of reservoir brine for simplicity). Both Carter analytical and numerical reservoir flux models are valid in linear reservoir regime only, in which fluid streamlines are perpendicular to the fracture walls. Depending on parameters of reservoir and hydraulic fracture, linear filtration regime can be either very long (of order of year for very low-permeability formations) or very fast (for high-permeability formations). Using the approach on determining the duration of filtration regimes in fractures reservoirs formulated in Economides and Nolte (2000), we conclude that the typical duration of linear filtration regime in Achimov terrigenous reservoirs of Western Siberia is in the range in between two weeks and a month.

In the current study we assume that at the initial time instant the pressure in the reservoir and hydraulic fracture is uniform. At each time step, the numerical coupling in between hydraulic fracture and reservoir filtration models is as follows: (i) solve numerically Eqs. (42), (46) and (50) formulated for reservoir parameters at current boundary conditions (i.e., distribution of pressure inside the hydraulic fracture and pore pressure at external reservoir boundary): to obtain the filtration velocity at the fracture walls (q_2 in Eq. (42) describing filtration in the fracture); solve numerically Eqs. (42)–(50) describing filtration in the fracture to update distribution of pressure; (iii) repeat steps (i) and (ii) until convergence criterion is met:

$$\frac{\|p^s - p^{s-1}\|}{\|p^s\|} < \epsilon_{tol}$$

where s is the number of fixed-point iteration at each time step; p is the vector composed of pressure values approximated at mesh nodes; $\|\cdot\|$ is a certain norm (e.g., L_2 or L_∞) and ϵ_{tol} is a convergence tolerance.

Numerical solution to the filtration equations both in the hydraulic fracture and in the reservoir is obtained using IMPES method (implicit pressure explicit saturations) and finite difference approximation at staggered uniform grid. The implemented numerical algorithm is also used in Redekop et al. (2021), in which the mesh convergence is shown. Influx form reservoir is calculated only in several mesh nodes (test numerical calculation showed that the flux from reservoir have to be calculated at least in 3 nodes distributed uniformly along the fracture to preserve the accuracy of calculations of around 1%). Influx in the rest of mesh nodes is calculated using the linear interpolation.

3.2. Numerical simulations of fracture flowback

3.2.1. Modelling of the flow in hydraulic fracture with a non-uniform proppant distribution

In this subsection we present the result of simulations of flowback in a hydraulic fracture filled heterogeneously with proppant in the form of isolated pillars according to the model formulated in Section 2.1.

For test purposes we consider the following artificial example: fracture length $L = 10$ m, distance between pillars is 0.25 m, length of pillars is 1 m; initial fracture aperture is $w = 5 \times 10^{-3}$ m. The rest of input parameters are shown in Table 1.

Inside the pillars, the proppant pack is subject to compaction and embedment into fracture walls according to Eqs. (48), (49) and Table. 7 (see Appendix 1). In between pillars, fracture opening is described according to Eq. (8), porosity is set to 1 and permeability corresponds to the one of a plane channel with Poiseuille velocity profile Witherspoon et al., 1980:

$$k = \frac{w^2}{12} \tag{54}$$

Note that in the derivation of geomechanics model for the fracture closure in between proppant pillars described by Eqs. (8) - (10), pressure is assumed to be constant along the fracture, while this is not the case for fracture flowback. We assume that the pressure does not vary significantly along the pillars l as introduced

Table 1
Parameters of fracture, reservoir and fluids.

Parameters and dimensions	Values
Fracturing fluid density, kg/m³	1000
Fracturing fluid plastic viscosity, Pa·s	0.4×10^{-3}
Irreducible frac. fluid saturation in reservoir	0.39
Irreducible oil saturation in reservoir	0.32
Initial pressure in fracture and reservoir, Pa	3.55×10^7
Final pressure in wellbore, Pa	2.55×10^7
Fracture height, m	16
Initial fracture width, m	5×10^{-3}
Initial fracture permeability, m²	1.082×10^{-9}
Initial fracture porosity	0.426
Reservoir porosity	0.07
Fracturing fluid compressibility, 1/Pa	4.4×10^{-10}
Oil compressibility, 1/Pa	1×10^{-9}
Reservoir Poison coefficient	0.2575
Reservoir Young module, Pa	1.675×10^7
Principal stress in reservoir, Pa	-6.81×10^8
Reservoir internal friction angle, degree	62.2
Reservoir friction coefficient	0.25
Rock cohesion, Pa	3.6×10^7
Proppant radius, m	0.5×10^{-3}
Reservoir permeability, m²	0.986×10^{-15}

in Section 2.1, which is valid if $l \ll L$, where L is the fracture length or height scale.

We carried out calculations with the pressure drop of 5×10^6 Pa in a wellbore, which is developed during 0.5 day. The duration of flowback process calculated is 3 days. Our goal is study the effect proppant pack deformation on fracture closure in between pillars as described by Eqs. (8) and (9), the results of calculations are shown in Fig. 18.

We obtained that the difference between the fracture aperture described by models descibed by Eqs. (8) and (9) is not significant in case of 5×10^6 Pa pressure drop (blue and green curves almost coincide in Fig. 18a). Fracture closure in between proppant pillars is most pronounced in the vicinity of the wellbore, whereas the closure of a fracture filled by proppant pillars does not change significantly along its length.

We also carried out calculations of fracture flowback at the larger instant bottomhole pressure drop of 10^7 Pa (Fig. 18b). For simplicity, we do not take into account compaction and embedment of proppant pillars (parameters ϵ_{33} and e_0 are set to zero in Eqs. (48) and (49)). The difference between the models of fracture closure in between pillars defined by Eqs. (8) and (9) is still insignificant and does not affect total oil production. Therefore, for fracture flowback modelling using parameters from Table 1, we can use the simplified model of fracture closure described by Eq. (9).

3.2.2. Effect of the bottomhole pressure drop dynamics on the fracture cleanup and oil production

There are three major competing factors affecting fracture conductivity degradation during flowback, namely, geomechanics, influx from reservoir and yield stress of unbroken hydraulic fracturing gel. In terms of geomechanics, the highest oil production can be achieved during a slow pressure drop to prevent non-elastic deformation of the pack (especially, for sand proppant grains) and rock formation (proppant embedment and tensile failure). In terms of the influx from the reservoir and the yield stress of the fracturing fluid, on the contrary, a rapid pressure drop leads to higher oil production.

We perform parametric study of fracture flowback to find the optimum wellbore pressure drop scenario to obtain the highest oil production. A number of calculations is carried out with different initial values of dimensionless fracture conductivity ($C_{FD} = k_f w/$
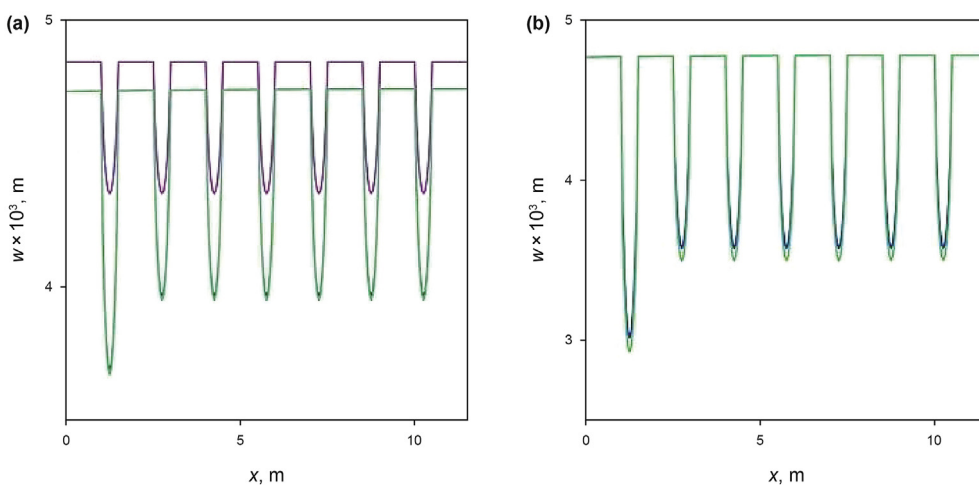

Fig. 18. Distribution of aperture (in millimeters) along the fracture filled with proppant pillars; initial aperture is shown by purple curve; green curve shows the fracture aperture, in which deformation of fracture walls in between pillars is calculated using Eq. (8) (pack deformation is taken into account), while the blue one corresponds to the model Eq. (9), in which proppant deformations are ignored; in plot (**a**), bottomhole pressure drops by 5×10^6 Pa during 0.5 days and deformation in fracture zones filled with proppant are taken into account; in plot (**b**), pressure drops by 10^7 Pa instantaneously and deformation in fracture zones filled with proppant are ignored.

($k_r x_f$)), which is typically used to evaluate steady-state production regime in fractured wells. We also evaluate the effect of yield stress of unbroken cross-linked gel ($\tau_y = 1$ Pa) and compare the results against the simulations of flowback in the hydraulic fracture filled initially with a Newtonian fluid ($\tau_y = 0$). In the simulations, reservoir permeability is varied in the range from 0.986×10^{-18} m^2 (0.01 mD) (very tight sandstone) to 0.986×10^{-12} m^2 (1 D) (high-permeable sandstone), initial fracture width is 3×10^{-3} m and 5.78×10^{-3} m, fracture length is 157 and 250 m. We consider three pressure drop scenarios: a linear decrease during 2 h, 1 day and 7 days by 10^7 Pa with respect to an initial reservoir pressure. The flowback period, after which we evaluated the production, is set to 100 days. The rest of the parameters are shown in Table 1.

To determine the optimal pressure drop scenario, we introduce a parameter ΔQ which is the ratio of oil production from the fracture calculated at the pressure drop either during 1 day or 7 days (moderate and slow cleanup) to that during 2 h (fast or aggressive cleanup):

$$\Delta Q = \frac{Q_{1d/7d}}{Q_{2h}} \times 100\% \tag{55}$$

Here Q_{2h} and $Q_{1d/7d}$ are volumes of oil produced during 100 days from the hydraulic fracture with bottomhole pressure drop during 2 h, 1 day and 7 days, respectively. The results of calculations of relative production volumes with different initial C_{FD} are presented in Fig. 19. According to the definition of parameter ΔQ, values $\Delta Q <$ 100% correspond to the case when fast cleanup (bottomhole pressure drops during 2 h) provides higher oil production as compared to that in fractures with the moderate or slow cleanup (bottomhole pressure drops during 1 day or 7 days), while if $\Delta Q > 100\%$, the

moderate or slow cleanup are preferable in terms of the total oil production.

When the fracturing fluid is viscous (yield stress is zero, see Fig. 19a), the plot can be divided into four sections with qualitatively different behaviour of oil production with respect to a change in the bottomhole pressure drop dynamics: for $C_{FD} > 13$, the fastest pressure drop scenario (aggressive cleanup) is preferable; for $2 < C_{FD} < 13$, the optimal pressure drop time period is in between 2 h and 7 days (moderate cleanup). For $1.3 < C_{FD} < 2$, the slowest pressure drop scenario is the best (slow cleanup); and for $C_{FD} < 1.3$, the moderate cleanup (during 1 day) is preferable.

If the fracture is filled initially with unbroken cross-linked gel (yield stress is 1 Pa, see Fig. 19b), we also found four qualitatively different regions in the plot of ΔQ against C_{FD}: for sufficiently large initial dimensionless fracture conductivity ($C_{FD} > 13$), the fastest pressure drop scenario is most effective; for $1.3 < C_{FD} < 13$, the slowest rate of pressure decline provides the highest oil production; for $0.13 < C_{FD} < 1.3$, the moderate slow pressure drop is preferable; for $C_{FD} < 0.13$, the fast pressure drop provides the highest oil production.

Dimensionless fracture conductivity C_{FD} is not an independent non-dimensional parameter determining the flowback process described by the coupled "fracture-reservoir" model (see Section 3.1). There are four dimensionless parameters, describing hydrodynamics as defined below:

$$N_k = \frac{k_r}{k_{f0}}, \quad N_g = \frac{L}{w_0}, \quad N_y = \frac{\alpha \tau_y L}{\Delta p}, \quad N_{Sh} = \frac{T_{sc}}{T_{drop}} \tag{56}$$

where Δp is total (maximum) bottomhole pressure drop; T_{drop} is a time scale of bottomhole pressure decrease; T_{sc} is hydrodynamic
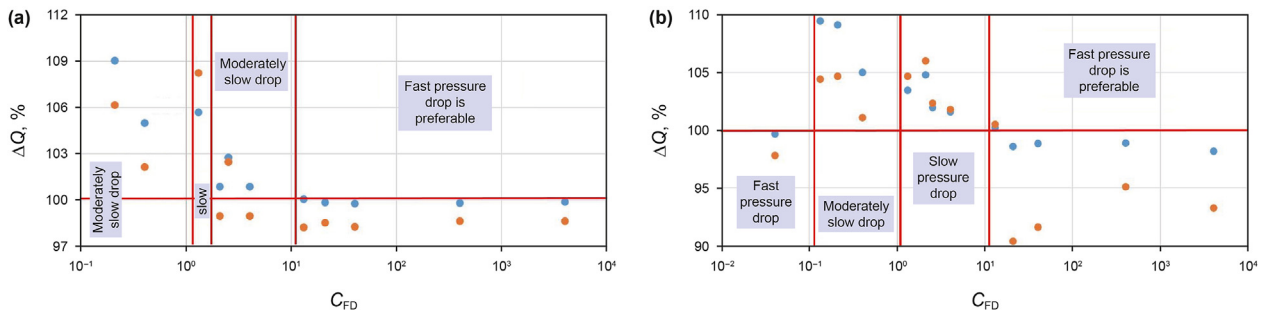

Fig. 19. Relative oil production ΔQ against initial dimensionless fracture conductivity C_{FD}. Plots (**a**) and (**b**) correspond to $\tau_y = 0$ and 1 Pa, respectively; by blue dots we show relative oil production change with the pressure drop maintained during 1 day, while orange dots correspond to that during 7 days.
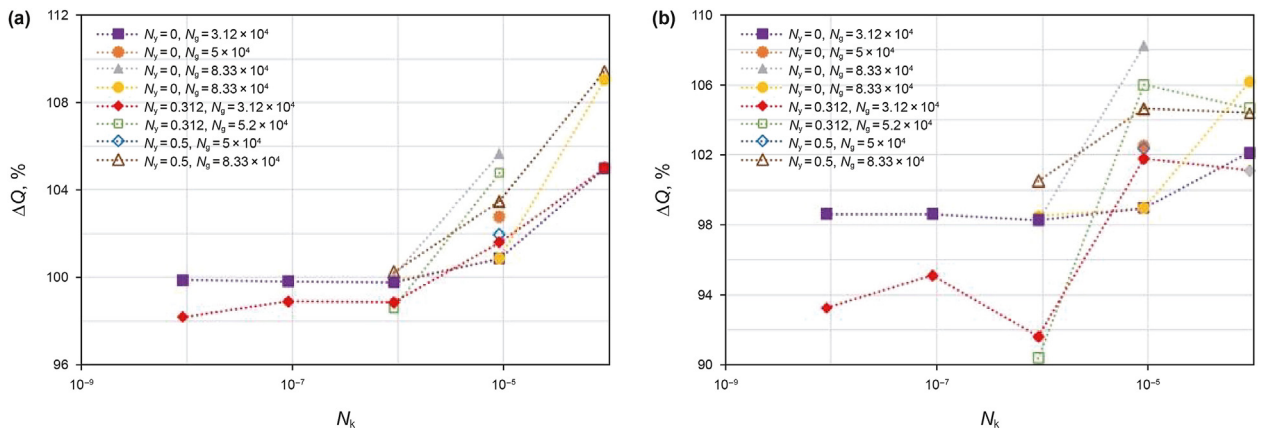

Fig. 20. Relative oil production ΔQ against reservoir-to-fracture permeability ratio evaluated at the start of flowback N_k. Calculations with pressure drop in 1 day (**a**) and 7 days (**b**).
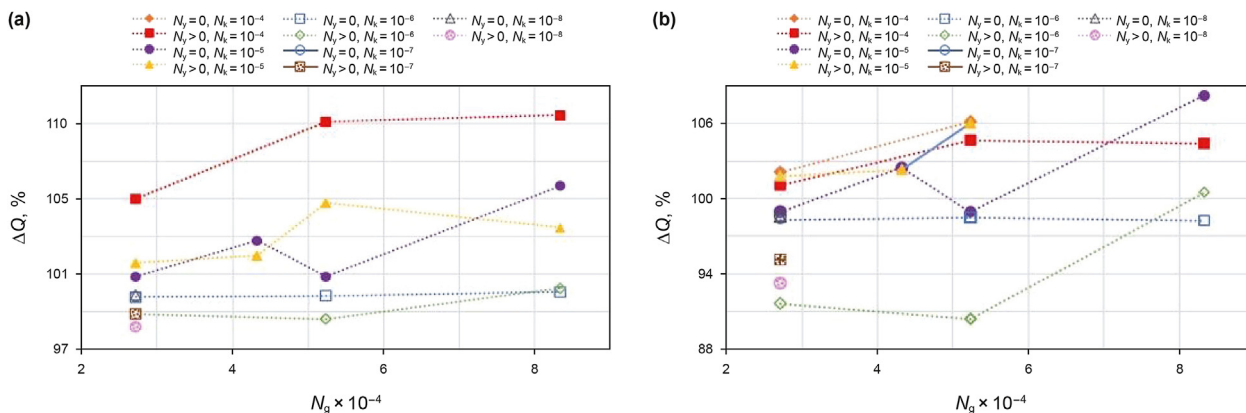
Fig. 21. Relative oil production ΔQ vs initial N_g. Calculations with pressure drop in 1 day (**a**) and 7 days (**b**).
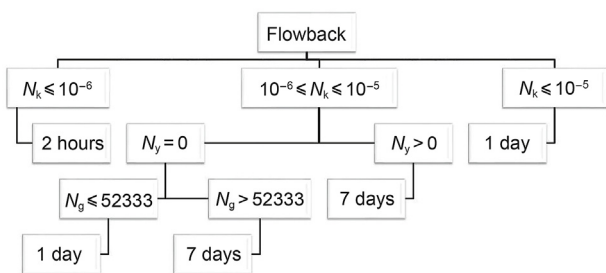

Fig. 22. Scheme for choosing the best pressure drop scenario.

time scale calculated using velocity and length scale of the problem (see below); N_k is the ratio of initial fracture permeability to the reservoir permeability; N_g is the fracture geometric parameter, the ratio of fracture length to the average initial aperture ($C_{FD} = 1/(N_k N_g)$); group N_y is the dimensionless critical pressure gradient determined by the yield stress of the fracturing fluid; and N_{Sh} is the Strouhal number determining the ratio of the hydrodynamic time scale to the time scale determining the dynamics of boundary conditions (i.e., time interval of bottomhole pressure drop). Parameters defined by Eq. (56) enter non-dimensional formulation of flowback problem described by Eqs. (42)−(50) obtained using the following procedure: fracture aperture w^* is scaled with the average initial aperture w_0, pressure p^* is scaled with total (maximum) bottomhole pressure drop Δp, filtration velocity u is scaled with velocity U determined according to Darcy law for filtration of oil and hydrodynamic time scale of the problem T_{sc} is determined according to the fracture length and velocity scale U as follows:

$$p^* = \frac{p - p_w}{\Delta p}, \ U = \frac{k_{f,0}}{\mu_2} \frac{\Delta p}{L}, \ T_{sc} = \frac{\varphi_0 L}{U} = \frac{\varphi_0 L^2 \mu_2}{k_{f,0} \Delta p}. \tag{57}$$

Complete set of non-dimensional parameters determining the flowback process described by Eqs. (42)−(50) also includes dimensionless compressibilities of fluids, fracturing fluid-to-oil viscosity ratio, reservoir brine-to-oil viscosity ratio and the set of parameters determining geomechanical processes. As these parameters usually do not vary significantly at the scale of a single oilfield, we do not consider their effect on fracture cleanup in the framework of parametric study.

The dependence between relative oil production and parameter N_k is presented in Fig. 20.

We obtained that for $N_k \leq 10^{-6}$ fast pressure drop is preferable;

for $N_k > 10^{-5}$, pressure drop during 1 day always provides higher oil production, and for N_k in between 10^{-6} and 10^{-5}, the pressure drop during 7 days is always preferable in case of the yield-stress fracturing fluid with $\tau_y = 1$ Pa.

We also studied the dependence between ΔQ and dimensionless geometric parameter N_g at a fixed value of N_k (Fig. 21).

The main trend shown in Fig. 21 is an increase in ΔQ with an increase in N_g. In the case of a viscous fracturing fluid (zero yield stress), when $N_k = 10^{-6}$, 1 day-long pressure drop period is preferable if $N_g \leq 5.2 \times 10^4$, and 7 day-long period provides the best results when $N_g > 5.2 \times 10^4$.

The results of parametric study can be summarized in a single scheme for choosing the best pressure drop scenario to obtain the highest oil production depending on the values of dimensionless parameters N_k, N_g and N_y (see Fig. 22).

3.2.3. Evaluation of tensile rock failure during fracture cleanup

In this section we evaluate tensile rock failure accompanying the flowback, which is rock disintegration due to excessive stretching strain of formation in the vicinity of a hydraulic fracture during a rapid pressure drawdown, the corresponding model is described in Section 2.3. Note that the model is one-way coupled with the model describing filtration in a proppant pack, so that it does not affect the flowback process in the current version of model described by Eqs. (42)−(50); it is used to evaluate qualitatively (i.e., whether the effect occurs or not) the negative effect of the rock failure on a flowback during a certain pressure drawdown.

Using the values of input parameters shown in Table 1, we calculate the threshold pressure drop Δp_s determining a plastic deformation of fracture walls leading to the tensile rock failure. We obtained that $\Delta p_s = 4.04 \times 10^7$ Pa for initial rock pore pressure of 3.55×10^7 Pa and 4.37×10^7 Pa for the minimum rock pore pressure of 2.55×10^7 Pa reached at the end of cleanup. A typical pressure drop during fracture flowback in Achimov formation of Western Siberia, Russia, is 1.5×10^7 Pa. Therefore we conclude that tensile rock failure does not occur during flowback process running at conditions described in Table 1.

3.3. Integrated well stimulation and production modelling: hydraulic fracturing − fracture cleanup − production

Routine modelling of production from hydraulically fractured wells carried out by petroleum engineers starts with simulations of hydraulic fracturing process using commercial software. The simulated geometry and conductivity of a propped fracture are required to model the long-term production, which, in turn, is

carried out using a hydrodynamic reservoir simulator. The standard simulation workflow does not include modelling of a fracture cleanup with accompanying dynamics of the fracture conductivity due to hydrodynamical and geomechanical effects described in preceding sections.

3.3.1. Description of integrated modelling workflow

The fracture flowback model described above assumes simplified description of the flow in a surrounding reservoir including a linear filtration regime and uniform reservoir properties. It allows to investigate a dynamics of the fracture conductivity only during a limited fracture cleanup period.

To investigate the effect of the fracture conductivity degradation during a flowback on long-term production running beyond formation linear filtration regime, we integrated the fracture flowback model described above into the well production simulation workflow as presented in Fig. 1. A similar idea of integrated design of fracture flowback - production is discussed in a chain of papers by Potapenko et al. (2017, 2019); Chuprakov et al. (2020); Potapenko et al. (2020).

Hydraulic fracturing process is simulated using Planar3D ILSA model taking into account layered structure of the reservoir with a contrast of geomechanics properties and 2D proppant transport model taking into account gravitational convection and proppant settling (Erofeev et al., 2019; Dontsov et al., 2019; Valov, 2021). The resulting geometry of a propped fracture as well as 2D distributions of fracture permeability and aperture along the fracture plane are used as input data for fracture flowback modelling.

At the next step, 2D distributions are converted into 1D ones by averaging over the fracture height to meet the limitations of the flowback model described by Eqs. (42)–(50). The obtained distributions are used as initial conditions for the flowback simulator. Note that in order to preserve the stability of the numerical algorithm, areas of fracture with low permeability (below 0.986×10^{-20} m^2 or 10^{-8} D) and width (below 0.8×10^{-3} m) are considered to be non-productive. Also, a predefined dynamics of the bottomhole pressure is required to set the boundary condition at well perforations. At the current stage, we set a certain dynamics of bottomhole pressure (BHP) measured in the field data. In our future studies, we plan to develop a coupled fracture flowback-wellbore model, which allows to calculate the dynamics of BHP using the dynamics of surface choke opening.

As a result of fracture flowback simulations, we obtain modified 1D distributions of fracture aperture and permeability, which allow calculating coefficients describing relative change of fracture permeability and aperture as follows:

$$C_{k,i} = \frac{k_i}{k_{0,i}}, \ C_{w,i} = \frac{w_i}{w_{0,i}}, \ C_{k,i}, C_{w,i} \in [0, 1]; \ 0 \le i \le N, \tag{58}$$

where k_{0i}, w_{0i} are initial fracture permeability and aperture for i-th grid cell along the fracture half-length; k_i, w_i are corresponding properties evaluated at i-th cell along the fracture half-length obtained using fracture flowback model (Eqs. (42)–(50)) and N is the number of mesh cells.

To modify the fracture two-dimensional fields, these coefficients are replicated over the fracture height in each cell of 2D computational grid. The final fracture permeability and aperture distributions are calculated as a product of two 2D fields, namely, initial fracture conductivity properties and modifying coefficients as follows:

$$k_{ij} = C_{k,i}k_{0,i}s_{o,i}, \ \ w_{ij} = C_{w,i}w_{0,i}s_{o,i}, \quad 0 \le i \le N, \ j \in \left[y_{b,i}, y_{t,i} \right],$$
$$\tag{59}$$

where $s_{o,i}$ is the oil saturation evaluated at the i-th cell along the fracture half-length; $y_{b,i}$ and $y_{t,i}$ are coordinates of the fracture bottom and top at the i-th cell along the fracture length. We multiplied the coefficients by the oil saturation to account for immobile fracturing fluid due to an insufficient pressure gradient (unyielded zones in unbroken cross-linked fracturing fluid).

The next element in the simulation workflow is prediction of the long-term production using a hydrodynamic reservoir simulator. 2D fields of geometry and degraded filtration properties of a hydraulic fracture are used to predict the oil production during a certain time period. The reservoir simulator describes the three-phase filtration using dynamic 3D PEBI-grid (Filippov et al., 2020).

Note that the simulation chain described above can be used to maximize the long-term production. For instance, to increase the values of the modifying coefficients, we can adjust the hydraulic fracture design or change the surface choke strategy to alter the bottomhole pressure dynamics. We conducted a series of numerical calculations with different fracture designs to study the influence of flowback on the fracture conductivity degradation and the long-term production.

3.3.2. Numerical simulations of the long-term production using the integrated modelling workflow

In the section we describe results of numerical simulations of the long-term production in fractured wells with flowback modelled according to the model described above. In contrast to the results of parametric study shown in Section 3.2, the production is described using a 3D reservoir simulator, so that the limitation of the reservoir filtration model to linear filtration regime is lifted. We study the effect of different factors accompanying flowback on a dynamics of the fracture conductivity and long-term production, namely,

- initial fracture aperture;
- diameter of proppant grains filling the fracture;
- yield stress of the fracturing fluid (unbroken cross-linked gel);
- dynamics of the pressure drop corresponding to different choke management strategies ("aggressive" and "slow" fracture cleanup regimes);
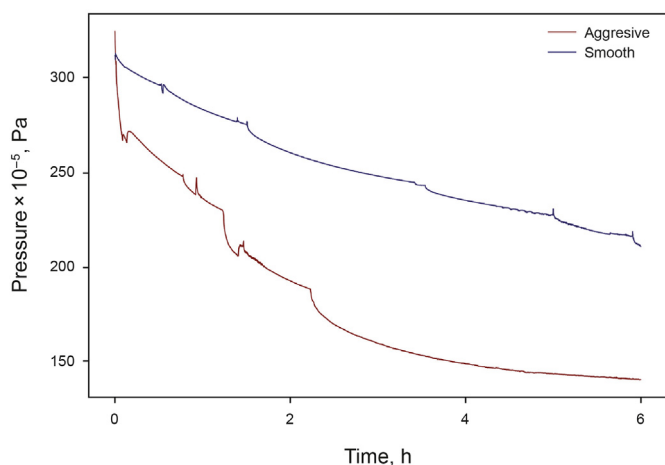- proppant material type (sand or ceramics).

Fig. 23. Examples of bottomhole pressure dynamics during aggressive (fast) and smooth (slow) flowback scenarios considered in the integrated well production simulations.

3.3.2.1. Input parameters. In the series of parametric calculations we set up a set of input parameters and only a single parameter is varied in each run as compared to the base case, while the rest of the parameters are fixed. Yield stress of the fracturing fluid is set to $\tau_y = 0.5$ Pa, which corresponds to the results of laboratory rheology measurements of unbroken gel used to create hydraulic fractures in Achimov formation of Western Siberia, Russia. We consider two bottomhole pressure dynamics obtained from field measurements during cleanup of oil wells, namely, aggressive (fast flowback) and smooth (slow flowback) as shown in Fig. 23; in the simulations we use the smooth bottomhole pressure dynamics unless stated otherwise. Also, by default, sand proppant particles are considered, for which dependence of pack permeability and aperture on confinement stress is described by the analytical model presented in Appendix 1 (see Eqs. (62), (63)).

Before describing the results of simulations, we comment on the organisation of figures shown below. In plots with 2D distributions of hydraulic fracture properties, horizontal coordinate shows the distance from one of the fracture tips. Fracture wings are assumed to be identical, so that well perforations are located in middle of the plot. In the figures showing the results of numerical simulations of long-term production carried out in reservoir simulator, "init" curve corresponds to an oil production obtained using the initial (i.e., not degraded) fracture permeability and aperture fields.

The long-term production period in the reservoir simulator is set to ten years. The well operates in a depletion mode with constant bottomhole pressure $p_{wf} = 8 \times 10^6$ Pa. There is the baseline fracture design with the medium width (2.5×10^{-3} m in average) and medium-sized proppant grains of fraction 16/20 mesh (with the mean grains diameter of around 10^{-3} m). The initial width and permeability distributions of the baseline hydraulic fracture are shown in Fig. 24.

3.3.2.2. Effect of the initial fracture aperture. Fracture aperture affects the fracture conductivity significantly. We varied the average initial fracture aperture from the narrow (1.25×10^{-3} m) to medium (2.5×10^{-3} m, see Fig. 24b) and wide (5×10^{-3} m). The calculated degraded 2D fracture conductivity fields suggest that the narrow fracture closes near the perforations during flowback and disconnects from the wellbore due to proppant embedment and proppant pack compaction effects (see solid blue curve in Fig. 25). The reason is that the pressure gradient near the perforations is the largest, which leads to the most pronounced effect of the proppant embedment and proppant pack compaction. We obtained that the fracture permeability increases with a decrease in initial fracture aperture, which can be explained by a lower velocity of transient pressure wave propagation in the narrow fracture as compared to the wide one (see Fig. 25a). Comparing the production from degraded fractures with different initial designs, we conclude that the wider the fracture, the less significant is the flowback effect on long-term production (Fig. 25b).
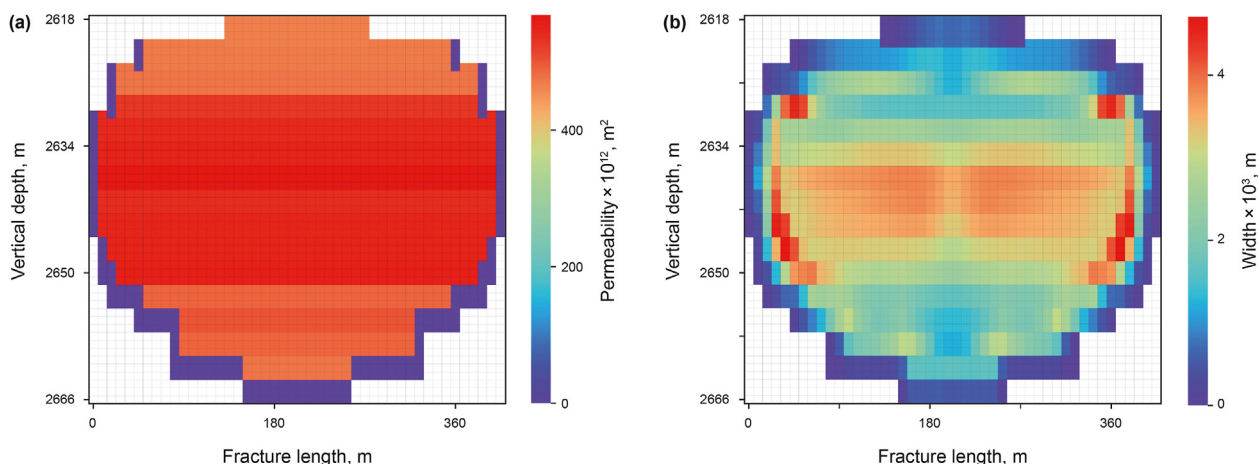
Fig. 24. Initial 2D distributions of the fracture permeability (**a**) and width (aperture) (**b**) for the fracture design with the medium (2.5×10^{-3} m) average aperture.

Fig. 25. Results of the reservoir production modelling: effect of the initial fracture aperture (small (1.25×10^{-3} m), medium (2.5×10^{-3} m) and large (5×10^{-3} m)) and the fracture conductivity degradation during a flowback on the long-term oil production.

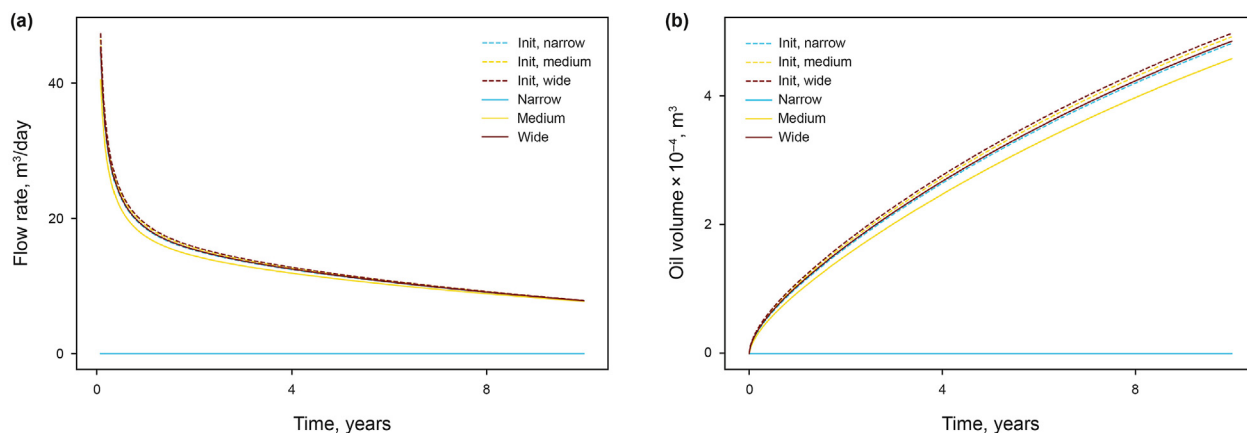*3.3.2.3. Effect of the proppant size.* Size of proppant grains is another important factor of fracture conductivity degradation. Usually, the larger the proppant grains, the higher the proppant pack conductivity due to wider pores. However, an increase in the particle diameter leads to an increase in their settling velocity, which limits their maximum transport length inside the fracture. More importantly, the proppant pack with large proppant grains is fragile since the contact areas of adjacent grains are small. The stresses applied to the pack can lead to proppant crushing and associated decrease in the fracture conductivity. In the fracture flowback model, the initial fracture porosity is calculated on the basis of the initial fracture permeability using Eq. (47). At the fixed confinement stress, the initial fracture permeability increases with an increase in the average diameter of the proppant grains. However, we fixed the initial fracture permeability distribution and varied only the proppant grains diameter with the aim to study the effect of the latter one on the long-term production at the fixed initial conditions. As the proppant embedment into the fracture walls is described by a semi-analytical model formulated in Eqs. (64)–(66), maximum embedment depth of a proppant grain is limited by its radius. We calculated the resulting 2D fracture properties and observed that the resulting fracture aperture for large proppant grains is smaller as compared to that obtained for small grains. Due to the fixed initial permeability, the initial

porosity is lower in the case of larger grains, so that the resulting permeability in this case is not larger than that in the case of small grains. The total volume of produced oil and oil flow rate are shown in Fig. 26.

3.3.2.4. Effect of the yield stress. In the third series of numerical simulations we study the effect of an initial yield stress of fracturing fluid τ_y on the fracture flowback and long-term production. The calculations are carried out for the design with the medium fracture aperture and proppant diameter (see Fig. 24). The length of the mobile fracture zone, in which the local pressure gradient is larger than the critical pressure gradient determined by the yield stress, decreases with an increase in τ_y, and the oil saturation factor introduced in Eq. (59) decreases with an increase in τ_y (Fig. 27). Conductive fracture aperture after flowback (calculated by the product of the calculated fracture aperture and oil saturation) also decreases with an increase in τ_y. In Fig. 28 we compare the long-term production of wells with fractures filled initially with an unbroken cross-linked gel. Both total oil production and oil flow rate curves show that an increase in the yield stress of a fracturing fluid leads to a decrease in the long-term oil production.

3.3.2.5. Effect of the bottomhole pressure dynamics. Next we study the effect of bottomhole pressure dynamics (smooth and aggressive
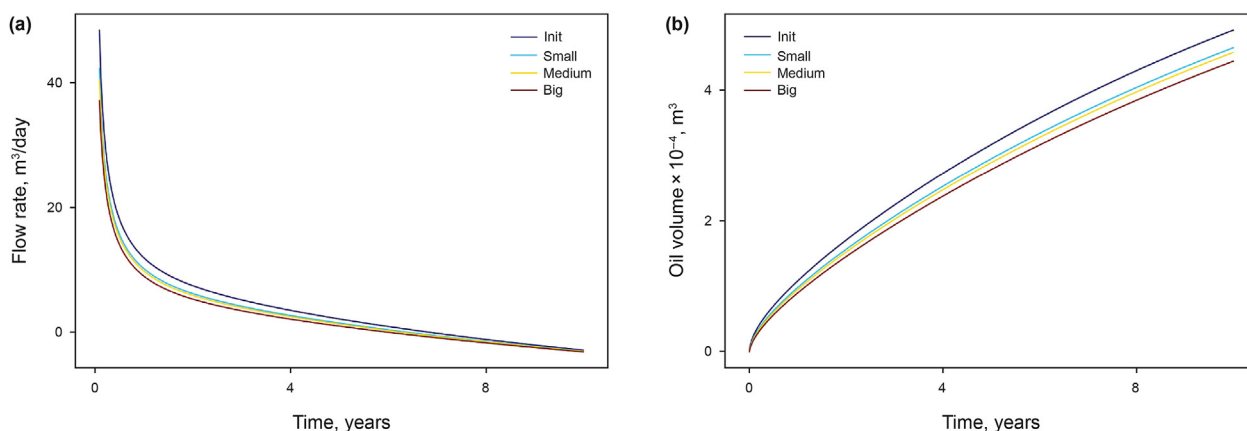
Fig. 26. Results of reservoir production modelling: effect of diameter of proppant grain on long-term oil production (the sieving meshes are 12/18, 16/20 and 30/60 for large, medium and small proppant grains, respectively).
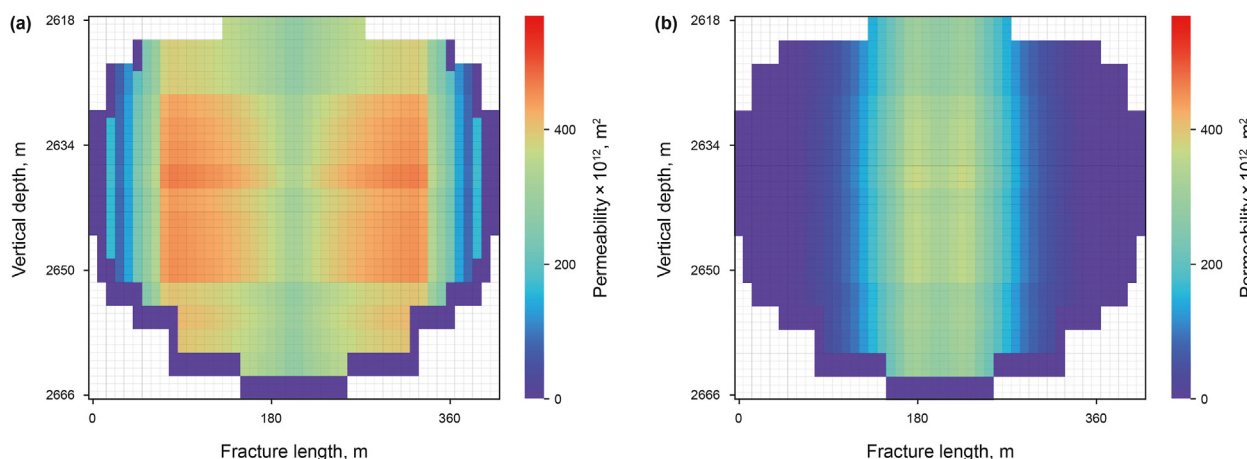
Fig. 27. Distribution of a degraded permeability after 6 days of flowback in the hydraulic fracture filled initially with an unbroken cross-linked gel with the yield stress of $\tau_0 = 0.5$ Pa (**a**) and 2 Pa (**b**).
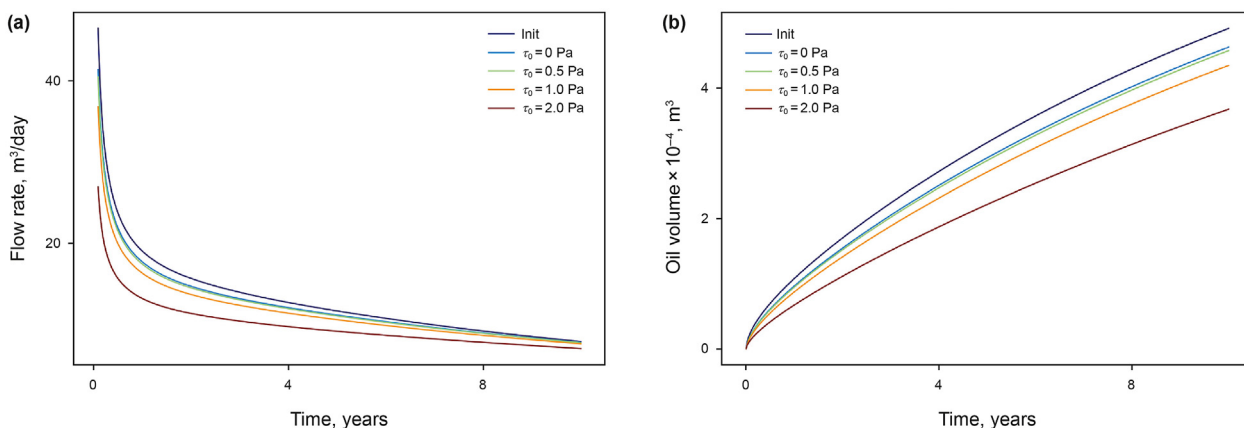
Fig. 28. Results of reservoir production modelling: effect of the yield stress of hydraulic fracturing fluid τ_0 on the long-term oil production.

as shown in Fig. 23) on long-term oil production at the yield stress of fracturing fluid set to 0.5 Pa. The degradation of the fracture permeability and aperture in the aggressive flowback scenario is more pronounced as compared to that obtained in the smooth scenario (compare Figs. 27a and 29). In the aggressive scenario, the

pressure gradient along the fracture is larger as compared to that in the smooth one. As a result, a damage to a near-perforation fracture zone in the aggressive scenario is more pronounced due to proppant pack compaction and embedment (corresponding oil production is shown in Fig. 30).
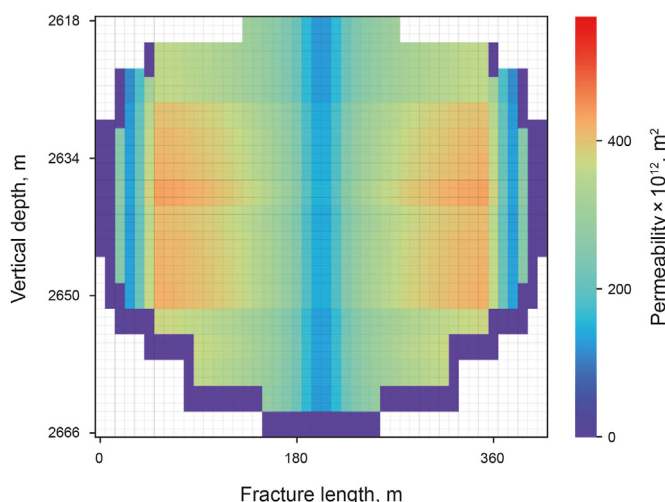
3.3.2.6. Effect of the proppant material. In the final set of simulations we study the effect of the proppant material on the fracture conductivity degradation and long-term production. While analytical expressions describing proppant pack compaction (see Eqs. (62) and (63)) are calibrated on a sand proppant by Zheng (2017), we consider compaction of aluminosilicate ceramic proppant via the results of standard laboratory measurements provided by proppant manufacturers. In our simulations we consider ceramic proppant of fraction 16/20 with the compaction measurements shown in Table 2. Dependence of the pack width on the

Fig. 29. Distribution of a degraded fracture permeability after 6 days of the aggressive flowback (bottomhole pressure corresponds to red curve in Eq. (23)) in the fracture with the medium average aperture 2.5×10^{-3} m).

Table 2
Laboratory measurements of permeability and width of aluminosilicate proppant 16/20-mesh pack at different applied stresses as considered in integrated numerical simulations of well production.

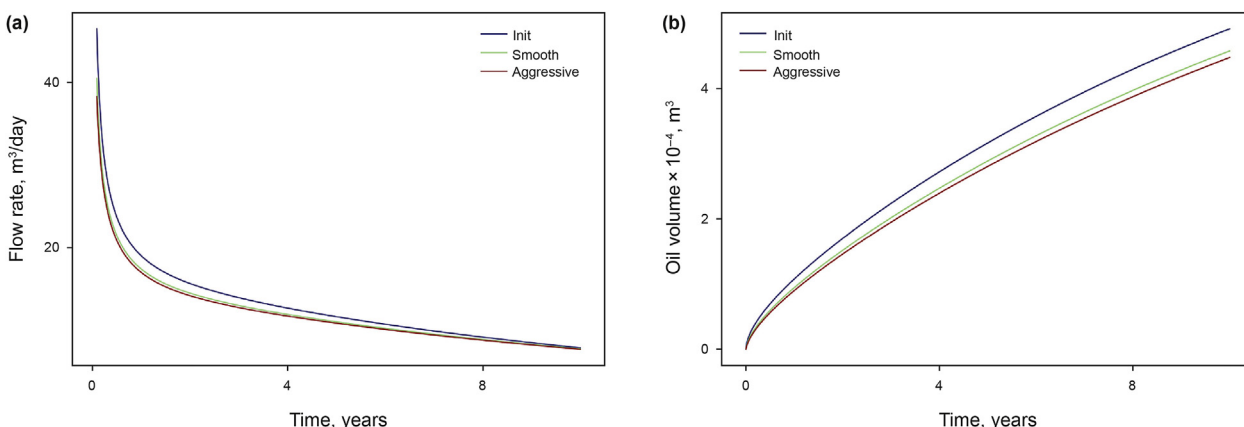| Stress $\times 10^{-7}$, Pa	Permeability $\times 10^{12}$, m^2	Pack width $\times 10^3$, m
1.36	1246	5.22
2.72	835	4.99
4.08	589	4.82
5.44	332	4.64
6.80	202	4.45

Fig. 30. Results of reservoir production modelling: effect of the bottomhole pressure dynamics (flowback aggressiveness, see Fig. 23) on the long-term oil production.

confinement stress allow calculating deformation ϵ_{33}, which is then used to calculate proppant pack porosity according to Eq. (49).

Ceramic proppant resists a large closure stress much more effectively as compared to a sand. Therefore, we expect a decrease in the degradation of the fracture conductivity as compared to that obtained for the sand proppant described above. We carried out simulations of the flowback in a hydraulic fracture filled with ceramic sand and corresponding long-term oil production, in which we varied the yield stress of a fracturing fluid. The comparison of the produced oil volume for the sand and aluminosilicate proppant in simulations with different yield stresses of fracturing fluid is shown in Fig. 31.

By results of integrated production simulations shown above we confirm that there are several critical factors affecting fracture conductivity dynamics during a flowback. A sub-optimal combination of input parameters (e.g., flowback dynamics, yield stress of fracturing fluid, proppant material) can lead to a significant fracture conductivity damage during fracture cleanup. As a result, the long-term oil production can be noticeably decreased (in particular, down to zero in case of fracture disconnection from the wellbore).

4. Evaluation of a fracture conductivity degradation using history-matched flowback model

The objective of this section is to compare the impact of geomechanics and rheology effects on oil production during limited flowback period using history-matched flowback model. We describe the method for estimation of production losses associated with inappropriate fracture clean-up procedure applied to four oil wells in Achimov formation of an oilfield located in Western Siberia, Russia, namely,

- Estimation of the fracture conductivity and effective fracture length after flowback;
- Estimation of production losses associated with a fracture cleanup performed outside of the safe operating envelope.

4.1. Adaptation of flowback model to field data

Two pairs of oil wells equipped with downhole gauges are chosen for field experiment to study the impact of a flowback
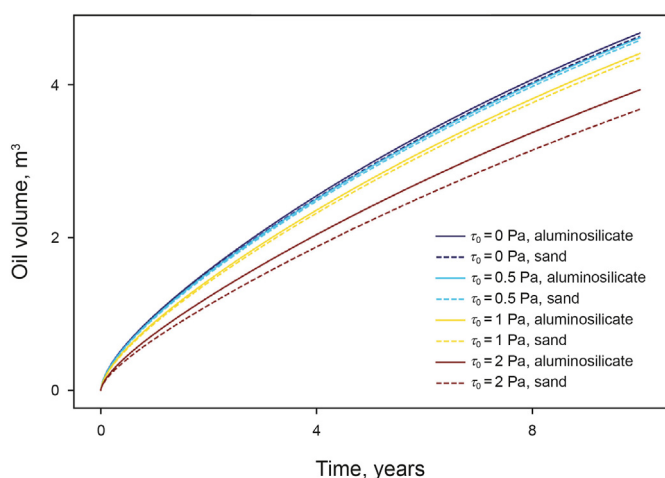
dynamics on the long-term production: two wells are cleaned up in an "aggressive" scenario and two wells in a "smooth" one. In order to compare the results of flowback, neighbour wells were selected from the same tight terrigenous sandstone oilfield (Achimov formation, Western Siberia, Russia) with similar reservoir properties. Design of field experiments and preliminary results of adaptation of the flowback model to field data are formulated in SPE conference proceedings (Osiptsov et al., 2019; Vainshtein et al., 2020; Vainshtein et al., 2021).

In this section we provide the results of a history-matching of the flowback model described above. Input data for flowback modelling includes: (i) reservoir properties determined from the core samples; (ii) rheology properties of fracturing fluids determined by laboratory measurements; (iii) fracture geometry and conductivity obtained using simulations of hydraulic fracturing calibrated at mini-fracturing stage; (iv) parameters of proppant pack compaction (i.e. dependence of the proppant pack aperture and permeability on the closure stress as supplied by manufacturer for ceramic proppant 16/20 mesh) and (v) wellbore pressure data obtained using bottomhole memory sensors.

4.1.1. Sensitivity analysis of the flowback to select tuning parameters of the matching procedure

Key tuning parameters for the history matching process are reservoir permeability k_r and yield stress of fracturing fluid τ_y, also we consider reservoir Young modulus and Poisson ratio to perform a sensitivity study and evaluate both fluid mechanics and geomechanics phenomena on the fracture conductivity dynamics during flowback. The choice is based on the uncertainty associated with determining these parameters and their influence on a key metrics that determine the well performance.

We carried out sensitivity analysis of well production by varying each of the parameters described above, with the rest of parameters being fixed (Figs. 32–34). In the plots, the horizontal axis shows the relative variation of a parameter as compared to the base case and the vertical axis shows the corresponding change in the chosen metric. The parameters of base case are shown in Table 3.

Fig. 31. Results of reservoir production modelling: produced oil volume of a well with attached hydraulic fracture filled with the sand and aluminosilicate proppant; the yield stress of a fracturing fluid τ_0 is varied in the range between 0 and 2 Pa.
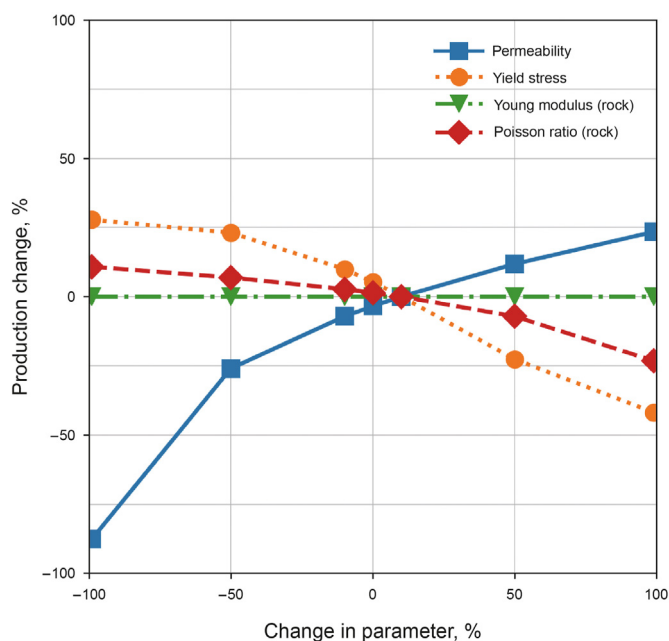

Fig. 32. Sensitivity of cumulative production of well 3 with respect to variation in the reservoir permeability, the yield stress of a fracturing fluid as well as the Young modulus and Poisson ratio of the rock (relative change).

Fig. 33. Sensitivity of the effective fracture length with respect to a variation in the reservoir permeability, the yield stress of a fracturing fluid as well as the Young modulus and Poisson ratio of the rock (relative change).

Fig. 34. Sensitivity of the dimensionless fracture conductivity C_{FD} with respect to a variation in the reservoir permeability, the yield stress of a fracturing fluid as well as the Young modulus and Poisson ratio of the rock (relative change).
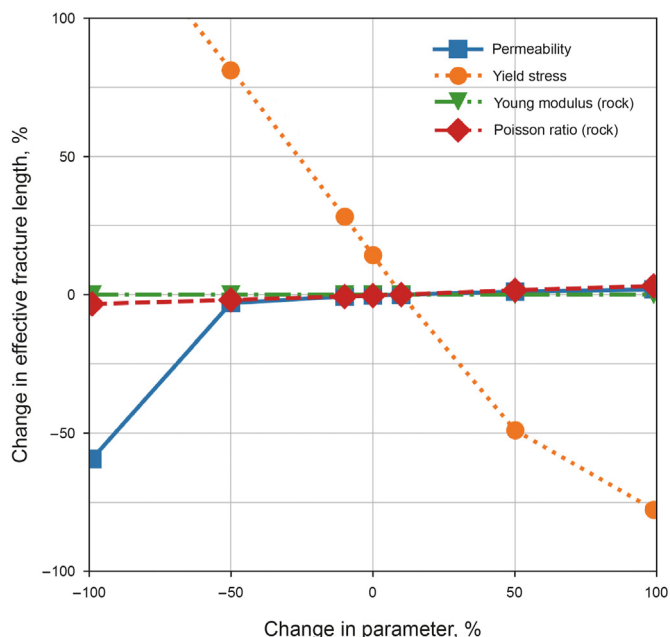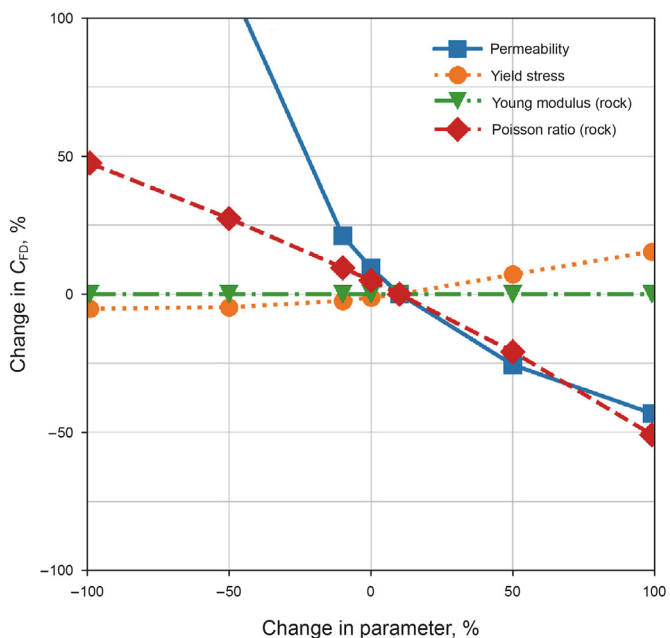
Table 3
Base values of parameters considered in the sensitivity study of flowback (well 3).

Parameter	$k_r \times 10^{12}$, m^2	τ_y, Pa	ν_s	$E_s \times 10^{-7}$, Pa
Value	1.38	2.0	0.25	1.625

Using the history matched fracture flowback model, we can estimate the dynamics of the fracture conductivity distribution

along its length. To take into account unyielded zones in the pore space occupied by a cross-linked gel, we calculate the effective (clean) fracture length x_{cf} defined as follows:

$$x_{cf} = \int_0^{x_f} s_2 \, dx \approx \sum_{i=1}^{N_{ns}} s_2(x_i)\Delta x$$

Here, x_f is an initial fracture length; x_i are coordinates of centers of mesh cells; $s_2(x_i)$ is corresponding oil saturation at the end of simulated time period; N_{ns} is a total number of mesh cells; $\Delta x = x_f/N_{ns}$ is the mesh step.

According to the sensitivity plot (Fig. 33), a significant effect on the effective fracture length is provided by the yield stress of a fracturing fluid τ_y and the reservoir permeability: note a significant decrease in the effective fracture length with a decrease in the rock permeability by two orders of magnitude as compared to its original value.

We also performed sensitivity study of the dimensionless fracture conductivity C_{FD} calculated after 30 days of flowback using the initial fracture length as well as the modified fracture aperture and permeability (Fig. 34). It is found that the most pronounced effect on C_{FD} is provided by the variation in the rock permeability and reservoir Poisson ratio, while that of the Young modulus and the yield stress is insignificant.

4.1.2. History matching of the flowback model

Reservoir permeability value is subject to a significant uncertainty as it needs to be determined separately for each hydraulic fracturing port and the number of corresponding measurements of rock properties is insufficient. At the same time, this parameter provides the most significant effect on cumulative production as it is shown in the sensitivity diagrams (Figs. 32–34).

Results of laboratory measurements on rheology of a cross-linked fracturing gel (specifically, the yield stress) can differ from that obtained at field conditions. Young modulus and Poisson ratio of the formation affect a proppant embedment into the fracture walls, and their variation can strongly affect the fracture conductivity during flowback. Additionally, values of geomechanical rock properties are usually difficult to determine accurately due to insufficient number of rock cores.

The history match is carried out in the following allowed range of variation of input parameters: $\pm$ 50% for rock permeability k_r and $\pm$ 60% for yield stress of the fracturing fluid τ_y. The control parameter is BHP, and the target match parameter is the liquid flow rate in reservoir conditions Q. The results of history matching of flowback model to field data related to the four wells under consideration are shown in Vainshtein et al. (2021), while here, for illustration, we show the history-matched results related to well 3 (see Fig. 35). Note that BHP values obtained using memory sensor were recalculated to surface conditions in accordance with an averaged true vertical depth of perforation interval assuming hydrostatics.

Dynamics of fracture properties for the history matched simulations of flowback in well 3 is shown in Fig. 36, we obtained that fracture width, permeability and porosity decrease towards well perforations as expected.

During flowback, the effective fracture length is reduced as compared to its initial value. In particular, the reduction is 15% for well 3 as shown in Fig. 37 due to a yield-stress rheology of the fracturing fluid.

The metric for evaluation of history matching results is MAPE (mean absolute percentage error) of the actual and simulated production rates in reservoir conditions. The values of MAPE for the matched model simulating 30 days of flowback are summarized in Table 4.
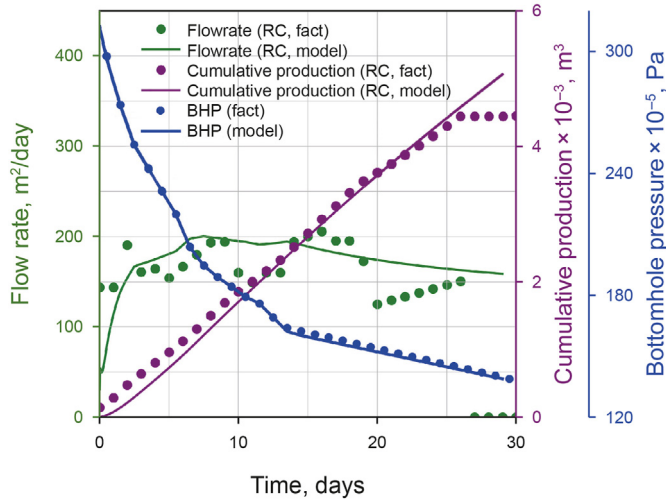
Fig. 35. The results of history matching of flowback model to field data related to well 3 (Vainshtein et al., 2021), the flowrate and cumulative production are shown in reservoir conditions.

4.2. Comparison of smooth and aggressive scenarios in terms of nondimensional metrics

To avoid ambiguous or misleading conclusions, we introduce non-dimensional metrics to compare "smooth" and "aggressive" flowback scenarios, namely, dimensionless productivity index J_d (Diyashev and Economides, 2006):

$$J_d = \frac{Q}{p - p_{wf}} \frac{\alpha_r B_f \mu}{kh},$$

where Q is a volumetric flow rate; p_{wf} is a bottomhole pressure; α_r is a constant; h is a fracture height; B_f is a formation volume factor.

Flowback effectiveness coefficient K_{Jd} is now determined as follows:

$$K_{Jd} = \frac{J_d}{J_d^0} \tag{60}$$

where J_d is a productivity index calculated using the fracture flowback model calibrated on field data and J_d^0 is obtained using flowback simulations, in which geomechanics effects of fracture conductivity degradation are ignored. According to Eq. (60),
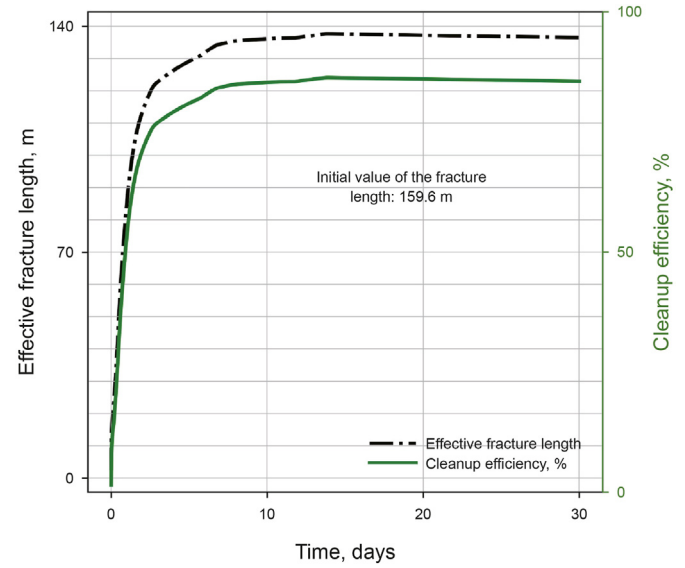
Fig. 37. Dynamics of the effective fracture length and cleanup efficiency (effective-to-initial fracture length ratio) during flowback in well 3 after Vainshtein et al. (2021).

Table 4
Evaluation of history matching using MAPE metric: deviation of actual flowrate from that obtained using flowback model developed in the current study.

Well	1-A	2-S	3-S	4-A
MAPE, %	7.53	36.44	12.25	22.66

parameter K_{Jd} can be calculated as the ratio of well flow rates with geomechanical effects turned on and off.

A diagram showing the proposed method for estimation of the flowback effectiveness coefficient is shown in Fig. 38.

A decrease in K_{Jd} corresponds to a fracture conductivity degradation due to negative impact of various factors on oil production. For all wells under consideration, we observe the same descending trend indicating degradation of fracture conductivity during 6 days of flowback (see Fig. 39). In these plots, the horizontal axis is the non-dimensional time scaled by parameter T_{sc} introduced in Eq. (57) and calculated for each of the wells separately: $T_{sc} = 1617$, 2610, 4307 and 2977 s for wells 1–4 under consideration, respectively. Note that rapid variations in the parameter K_{Jd} correspond to changes in pressure curve slope. By analysing the results we

Fig. 36. Distribution of the proppant pack permeability, porosity and aperture along the hydraulic fracture in well 3 after Vainshtein et al. (2021); plots (**a**) and (**b**) correspond to days 1 and 7 after the start of flowback, respectively.

conclude that geomechanical effects decrease the productivity index of the wells by about 20% in the first 6 days of flowback.

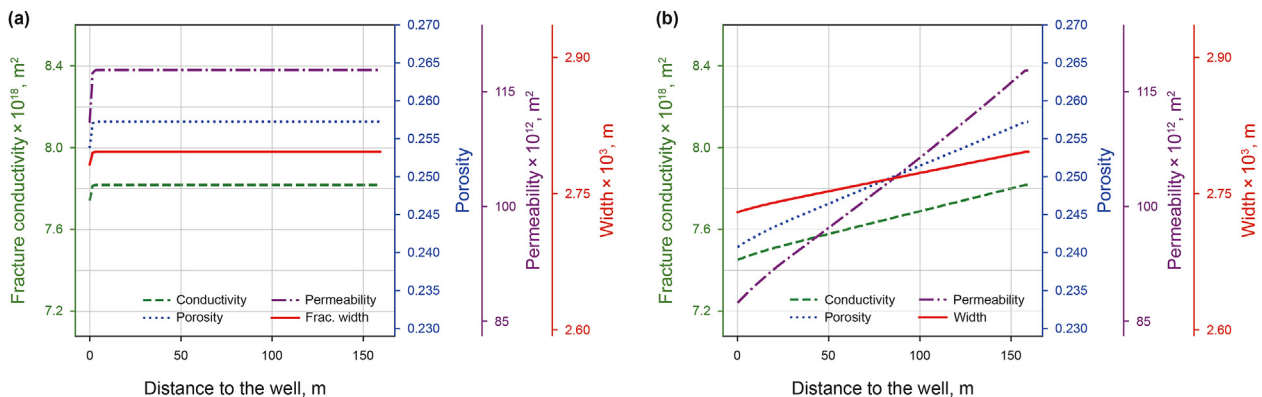As discussed in Section 3.1, the developed flowback model is applicable only to a linear flow regime in rock formation surrounding a hydraulic fracture, so that the dynamics of K_{Jd} in later (e.g., pseudo steady-state) regime cannot be obtained directly from the simulations. We consider the correlation presented in Cinco-Ley et al. (1981) between dimensionless fracture conductivity C_{FD} and productivity index J_d, calculated as follows:

$$J_d = \frac{1}{\ln(r_e/r_w) - 0.75 + S_f} = \frac{1}{\ln(r_e/r'_w) - 0.75}, \quad (61)$$

where the dependence of reservoir-to-effective well radii ratio r_e/r'_w on C_{FD} is shown in Cinco-Ley et al. (1981) in graphical form.

Equation (61) is valid for late flowback stages, when both the productivity and conductivity do not change significantly. Therefore,

the flowback efficiency coefficient K_{Jd} can be estimated using the following procedure: (i) we calculate the dimensionless fracture conductivity C_{FD} at the end of a formation linear regime using the flowback model (several weeks for well and reservoir parameters under consideration); (ii) corresponding value of $J_d(C_{FD})$ is calculated using correlation by Cinco-Ley et al. (1981); (iii) repeat steps (i) and (ii) for the simulations with fracture conductivity degradation effects switched off to obtain $J_d(C_{FD}^0)$. Calculated values of parameter K_{Jd} using the described procedure are shown in Table 5.

Results shown in Table 5 can be used to predict dynamics of hydraulic fracture productivity. Note that the fracture flowback efficiency does not drop below 80% as compared to the results obtained with geomechanical effects switched off, which is consistent with direct calculations of K_{Jd} shown in Fig. 39.

To conclude this section we discuss the dynamic similarity of a flowback process in the wells under consideration according to the non-dimensional problem formulation shown above in Section 3.2.2: key non-dimensional parameters are listed in Eq. (56). Pressure drop period T_{drop} is evaluated based on the dynamics of the non-dimensional bottomhole pressure p_{wf} (see Eq. (57)) as a function of the non-dimensional time t and determined according to the following condition:

$$\frac{dp_{wf}}{dt} = 10^{-3}.$$

We obtained that the flowback period for Well 1-A is 3 days, Well 2-S is 5 days, Well 3-S is 13 days and Well 4-A is 7 days. Calculated values of non-dimensional parameters defined by Eq. (56) are shown in Table 6. Note that values of parameters N_y and N_g are very close for the wells 1, 2 and 3, 4; the discrepancy is only in values of parameter N_k (rock-to-fracture permeability ratio), which are still of the same
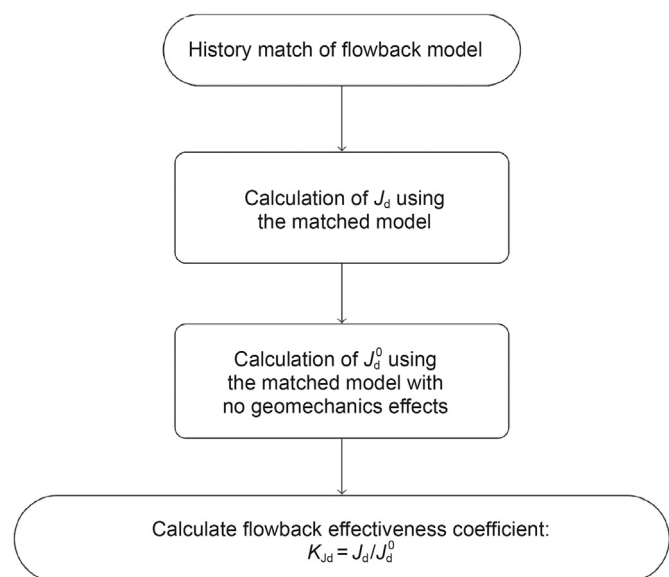
Fig. 38. A diagram depicting the method for estimation of flowback effectiveness coefficient considered in the current study.

Table 5
Daily averaged values of parameter K_{Jd} evaluated at day 6 after the start of flowback (see Eq. (60)).

Well	K_{Jd}
1-A	0.832
2-S	0.829
3-S	0.817
4-A	0.806
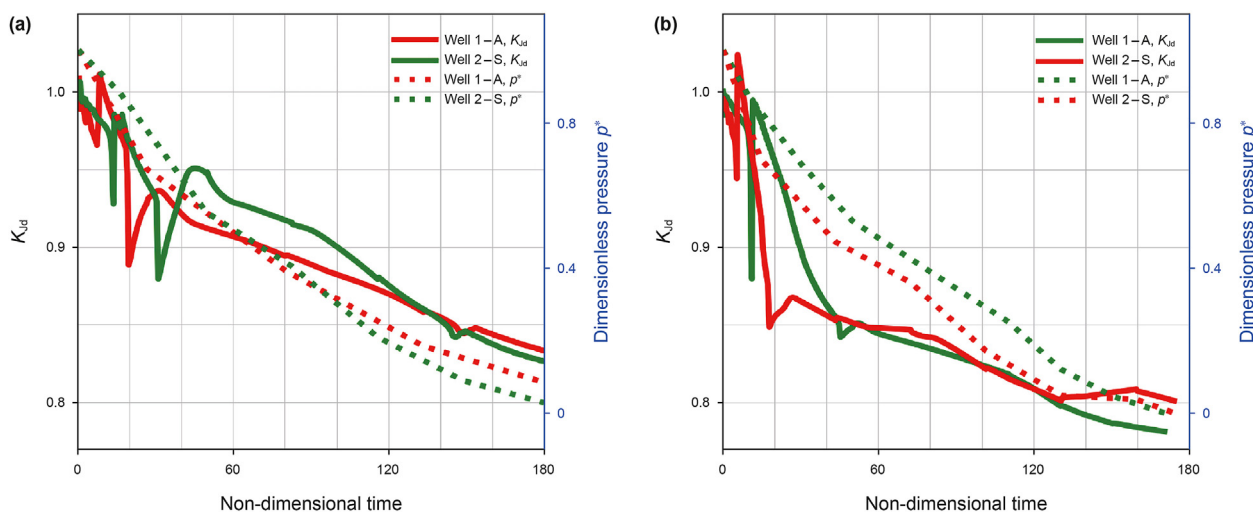
Fig. 39. Dynamics of the parameter K_{Jd} during first several days of flowback obtained using the method shown in Fig. (38); dashed lines correspond to p^*, solid lines correspond to productivity index; non-dimensional time and p^* are calculated using Eq. (57).

Table 6
Values of dimensionless governing parameters defined in Eq. (56) and calculated for flowback in wells 1—4 using original field data.

Parameter	Well 1-A	Well 2-S	Well 3-S	Well 4-A
N_y	0.328	0.348	0.551	0.605
$N_g \times 10^{-4}$	2.8	3.1	3.9	4.3
$N_k \times 10^7$	2.1	4.0	5	3.5
$N_{Sh} \times 10^3$	5.3	4.8	2.2	3.6

order of magnitude. Strouhal number N_{Sh} shows the effect of unsteady boundary conditions on the flow, so that a decrease in the Strouhal number corresponds to a decrease in the effect of unsteady boundary conditions on flowback. We obtained that the Strouhal numbers calcutaed for the parameters of wells 1 and 4 with aggressive flowback are larger as compared to those of smooth flowback (wells 2 and 3), which confirms that the surface choke opening strategy is chosen correctly and meets the goal of field experiments. As a result of non-dimensional analysis we conclude that there is a dynamic similarity in between flowback process running in wells 1, 2 and 3, 4 taking into account the total number of parameters determining the flowback process, so that we can evaluate the effect of flowback aggressiveness on oil production.

5. Summary and conclusions

In this work, we developed an integrated modelling workflow for transient flowback in hydraulically fractured wells. The fracture flowback model developed in the present study is extended in terms of new geomechanical and hydrodynamical flowback phenomena, as compared to our previous study (Osiptsov et al., 2020).

These phenomena include inhomogeneous distribution of the proppant in the fracture, resulting from alternate-slug fracturing, overflush, or proppant flowback. Hydraulic fracture closes on proppant-free cavities due to pressure drawdown and formation creep. The magnitude of fracture closure is evaluated for a proppant pillar as a half-space under boundary conditions of a specified stress inside the contour of the gap and zero vertical displacements outside of the contour. The solution is obtained under the assumption that the deformation of the proppant pack is ignored and that the proppant pack behaves as an elastoplastic body with a plastic zone developing at the contour of the gap. Ignoring elastic deformations, the dimensions of the plastic zone are determined similar to calculation of the plastic zone dimensions formed at the tip of the fracture. Then, using the solutions obtained for a flat and circular gaps, the displacement of fracture walls is determined. Elastic solutions are obtained, which allow taking into account the rock creep and determine the closure time.

Another risk associated with a pressure decrease in the fracture is the development of a plastic zone at the fracture walls, which gradually propagates into the rock. Plasticity and creep lead to micro-fracturing of the rock and alteration of its porosity and Carter's leak-off coefficient.

We implemented a yield-stress rheology of fracturing fluids to the flowback model with the aim to describe the effect of an unbroken cross-linked gel on a fracture cleanup. Note that hydraulic fracturing in shale formations is usually made using water with small amount of friction reducer additives (i.e., "slickwater"), so that the target application of the developed model is conventional fracturing with cross-linked fracturing fluids in traditional terrigenous oil reservoirs. Reservoir-to-fracture flux model is upgraded from analytical Carter's model to numerical two-phase filtration model in reservoir, which allows us to take into account transient pressure distribution along the fracture, displacement of leaked-off frac fluid into the formation and a non-uniform pressure distribution formed in the reservoir during hydraulic fracturing job.

For the parameters typical of oil wells in low-permeability Achimov formation of Western Siberia, Russia, we carried out parametric analysis of flowback scenarios. We studied the effect of key non-dimensional parameters determining a fracture flowback and a dynamics of a pressure drawdown on oil production. In particular, we identified ranges of dimensionless fracture conductivity, reservoir-to-hydraulic fracture permeability ratio, fracture length-to-aperture ratio and dimensionless critical pressure gradient, in which a certain flowback strategy (namely, aggressive, moderate or smooth) is recommended to maximize cumulative oil production.

The flowback model is integrated into the well production modelling workflow comprising simulations of hydraulic fracturing using Planar3D ILSA model and long-term production using a hydrodynamic reservoir simulator. The proposed simulation chain allows us to lift the limitation of a reservoir linear filtration regime of the developed standalone flowback model. We performed parametric study of the long-term oil production in a well taking into account fracture conductivity degradation during flowback for the parameters typical of Achimov formation, Western Siberia. We obtained that at a fixed diameter of proppant grains, an increase in the mean fracture aperture in the range between 1.25 and 5 mm, a decrease in the fracturing fluid yield stress from 2 to 0 Pa or switch from sand to ceramic proppant (at the fixed initial permeability) leads to an increase in cumulative oil production. We also studied the effect of flowback aggressiveness on the long-term oil production and obtained that a smooth flowback is more preferable.

We describe the history-matching of the flowback model to field data of four oil wells in Achimov formation. A single tuning parameter, namely, rock permeability, is chosen according to the sensitivity of the results of flowback simulations and uncertainty analysis of field data. The matched model allows evaluating the effect of geomechanical factors on fracture degradation using dimensionless flowback effectiveness coefficient. We obtained that proppant compaction and embedment decrease the flowback effectiveness by 20% after 6 days of fracture cleanup. Using the matched model, we can reduce the high uncertainty in an initial data due to the history matching procedure.

Finalization of flowback modelling workflow requires coupling of the fracture flowback model to a wellbore model to be able to calculate the dynamics of the bottomhole pressure at a specified strategy of choke opening at the surface. As for the further development of the fracture cleanup model, we believe that the polymer cake formed at fracture faces during an injection and a clogging of proppant pack pores with residue formed during breaking of cross-linked gel are important effects that need to be taken into account, which is planned for our future studies.

Appendix 1

Below we formulate proppant compaction and embedment models developed by Osiptsov et al. (2020).

The compaction takes into account a rearrange of proppant grains and dilatancy of the pack due to the confining stress and is

described by the following equation:

$$\Delta p_{\mathrm{s}} = \frac{E}{3(1-\nu^2)} \left(\frac{2A_{\mathrm{s}}}{3} \epsilon_{33} \left[1 - \frac{B_{\mathrm{s}}}{n_{\mathrm{s}}+1} \epsilon_{33}^{n_{\mathrm{s}}} \right] \right)^{3/2}, \tag{62}$$

$$A_{\mathrm{s}} = \left[1 - \frac{2}{3+2\alpha_{\mathrm{fr}}\Lambda} \left(1 - \frac{1}{\sqrt{3}}\Lambda \right) \left(1 - \frac{1}{\sqrt{3}}\alpha_{\mathrm{fr}} \right) \right], \tag{63}$$

where B_{s} and n_{s} are tuning parameters, E and ν are effective Young modulus and Poisson ratio of the pack, Λ is the dilatancy coefficient and α_{fr} is the internal friction coefficient of a pack.

For $E = 5 \times 10^{10}$ Pa, $\nu = 0.17$, $\alpha_{\mathrm{fr}} = 0.34$ and $\Lambda = -0.378$, the following values of free parameters allow to describe the laboratory data on compaction of sand pack shown in Zheng (2017) accurately: $B_{\mathrm{s}} = 56$ and $n_{\mathrm{s}} = 2$.

In the current study we also use an alternative approach to describe compaction of the pack of ceramic proppant using laboratory measurements provided by proppant manufacturers. Dependence of the fracture aperture and permeability on the confining stress used in the parametric study of flowback described in Section 3.2.2 is shown in Table 7. The compaction data allows calculating deformation of the pack ϵ_{33} and find the actual value of the fracture permeability during a flowback.

Table 7
Proppant passport data supplied by a manufacturer: dependence of pack aperture and permeability on the closure stress for 12/18 mesh ceramic proppant.

Stress $\times 10^{-7}$, Pa	Permeability $\times 10^{12}$, m^2	Pack width $\times 10^3$, m
1.36	879	5.56
2.72	646	5.34
4.08	318	5.06
5.44	151	4.77
6.80	72	4.56

Proppant embedment model was formulated for a layer of hard spheres, which embed into an elastoplastic semispace representing hydraulic fracture walls. The model is described by the following equation:

$$\Delta p_{\mathrm{s}} = p_{\mathrm{h}} - p_{\mathrm{f}}, \tag{64}$$

$$\Delta p_{\mathrm{s}} = \left(\frac{A_{\mathrm{e}}}{C_{\mathrm{e}}} [p_{\mathrm{h}} + (c\cot\varphi_{\mathrm{e}} - p_{\mathrm{r}})] - B_{\mathrm{e}} \right) \Big/ \left(\frac{L^2}{2\pi r^2} + \frac{A_{\mathrm{e}}}{C_{\mathrm{e}}} \right), \tag{65}$$

$$
\begin{aligned}
A_{\mathrm{e}} &= e^{2\theta_0\tan\varphi_{\mathrm{e}}} \left(2\tan\varphi_{\mathrm{e}}\cos^3\theta_0 + 3\cos^2\theta_0\sin\theta_0 \right) \\
&\quad + \frac{4\tan^2\varphi_{\mathrm{e}}+3}{4\tan^2\varphi_{\mathrm{e}}+1} e^{\tan\varphi_{\mathrm{e}}\pi} - \frac{4\tan^2\varphi_{\mathrm{e}}+3}{4\tan^2\varphi_{\mathrm{e}}+1} e^{2\theta_0\tan\varphi_{\mathrm{e}}}(2\tan\varphi_{\mathrm{e}}\cos\theta_0+\sin\theta_0), \\
B_{\mathrm{e}} &= \frac{1}{3}c\cot\varphi_{\mathrm{e}}\sin\varphi_{\mathrm{e}} \left(1 - \sin^3\theta_0 \right), \\
C_{\mathrm{e}} &= (1-\sin\varphi_{\mathrm{e}}) \left(4\tan^2\varphi_{\mathrm{e}}+9 \right), \\
\theta_0 &= \arcsin\sqrt{1-\frac{e_0}{r_{\mathrm{p}}}}.
\end{aligned}
\tag{66}
$$

where θ_0 is the embedment angle; c is the rock cohesion; φ is the internal friction angle of a rock; p_{r} is the pore pressure; r is the particle radius; and e_0 is the embedment depth.

Appendix 2

Expressions for coefficients in Eq. (4) are as follows:

$$E_{1111} = G\left\{ \left(\frac{4}{3} + \frac{K}{G} \right) - \frac{G}{G+\alpha\Lambda K} \left[-\frac{1}{\sqrt{3}}\,\mathrm{sgn}\left(\sigma_{22}^{\mathrm{eff}}\right) + \frac{K}{G}\Lambda \right] \left[-\frac{1}{\sqrt{3}}\,\mathrm{sgn}\left(\sigma_{22}^{\mathrm{eff}}\right) + \frac{K}{G}\alpha \right] \right\},$$

$$E_{2222} = G\left\{ \left(\frac{4}{3} + \frac{K}{G} \right) - \frac{G}{G+\alpha\Lambda K} \left[\frac{2}{3}\mathrm{sgn}\left(\sigma_{22}^{\mathrm{eff}}\right) + \frac{K}{G}\Lambda \right] \left[\frac{2}{3}\mathrm{sgn}\left(\sigma_{22}^{\mathrm{eff}}\right) + \frac{K}{G}\alpha \right] \right\},$$

$$E_{2211} = G\left\{ \left(\frac{K}{G} - \frac{2}{3} \right) - \frac{G}{G+\alpha\Lambda K} \left[\frac{2}{3}\mathrm{sgn}\left(\sigma_{22}^{\mathrm{eff}}\right) + \frac{K}{G}\Lambda \right] \left[-\frac{1}{\sqrt{3}}\,\mathrm{sgn}\left(\sigma_{22}^{\mathrm{eff}}\right) + \frac{K}{G}\alpha \right] \right\},$$

$$E_{1122} = G\left\{ \left(\frac{K}{G} - \frac{2}{3} \right) - \frac{G}{G+\alpha\Lambda K} \left[-\frac{1}{\sqrt{3}}\,\mathrm{sgn}\left(\sigma_{22}^{\mathrm{eff}}\right) + \frac{K}{G}\Lambda \right] \left[\frac{2}{3}\mathrm{sgn}\left(\sigma_{22}^{\mathrm{eff}}\right) + \frac{K}{G}\alpha \right] \right\}.$$

Appendix 3

Solution to the coupled pressure diffusion equations (see Eq. (35)) are obtained in the following form (Basniev et al., 2012):

$$p^{(1)} = A^{(1)} + B^{(1)} \text{erf}\left(\frac{x_3}{2\sqrt{\kappa^1 t}}\right),$$

$$p^{(2)} = A^{(2)} + B^{(2)} \text{erf}\left(\frac{x_3}{2\sqrt{\kappa^{(2)} t}}\right),$$

where $A^{(1)}$, $A^{(2)}$, $B^{(1)}$, $B^{(2)}$ are unknown constants, which should be determined using initial and boundary conditions. According to Eqs. (33) and (34), we obtain:

$$A^{(1)} = p, \quad A^{(2)} + B^{(2)} = 0, \tag{67}$$

$$A^{(1)} + B^{(1)} \text{erf}\left(\frac{x_3^{(1)}}{2\sqrt{\kappa^{(1)} t}}\right) = A^{(2)} + B^{(2)} \text{erf}\left(\frac{x_3^{(1)}}{2\sqrt{\kappa^{(2)} t}}\right) = p_{\text{pl}}. \tag{68}$$

From this condition, we find the solution for the self-similar coordinate, which in turn gives us the law of propagation of the plasticity front:

$$\frac{x_3^{(1)}}{\sqrt{t}} = \text{const} = \chi$$

or

$$x_3^{(1)}(t) = \chi\sqrt{t}. \tag{69}$$

Equation (69) is the law of plasticity front propagation: its co-ordinate is proportional to the square root of time, and the proportionality coefficient χ is an unknown constant to be found from the solution.

Using Eqs. (68), we obtain the following expressions for the constants:

$$B^{(2)} = -\frac{p_{\text{pl}}}{1 - \text{erf}(\chi/2\sqrt{\kappa^{(2)}})}, \quad B^{(1)} = \frac{p^{(2)} + p_{\text{pl}}}{\text{erf}(\chi/2\sqrt{\kappa^{(1)}})} \tag{70}$$

Thus, Eqs. (67) and (70) allow finding integration constants. In order to find the coefficient χ, we use Eq. (36). As a result, we obtain the equation

$$p^{(2)} = p_{\text{pl}}\left(1 - \text{erf}\left(\frac{x_3}{2\sqrt{\kappa^{(2)} t}}\right)\right)\left[1 - \text{erf}\left(\frac{\chi}{2\sqrt{\kappa^{(2)}}}\right)\right]^{-1}.$$

The front of plasticity $x_3 = x_3^{(1)}$ is moving with the following velocity, as follows from Eq. (69):

$$v_{\text{pl}} = \frac{\partial x_3^{(1)}}{\partial t} = \frac{\chi}{2\sqrt{t}}.$$

Nomenclature

Greek symbols

α	Internal friction coefficient
α_{fr}	Proppant friction parameter
α_y	Coefficient in formula for yield stress
β	Biot coefficient
β_i	Compressibility of i-th phase
δ_{ij}	Kronecher symbols
ε	Convergence criterion in coupled "hydraulic fracture-rock influx" numerical algorithm
ϵ	Bulk deformation (first invariant of strain rate tensor)
ϵ_{33}	Deformation of rock in direction perpendicular to the fracture face and deformation of proppant pack
ϵ_{ij}	Strain tensor components
ζ	Fluid content in the unit volume
η	Viscosity in the Maxwell model
θ_0	Embedment angle
λ	Lamé coefficients
Λ	Dilatancy coefficient
μ_i	Effective viscosity of i-th phase
ν	Poisson ratio
ν_s	Poisson ratio of rock
σ	Mean stress
σ_{11}^0	Initial stress
σ^{eff}	Effective mean stress
σ_{ii}	Components of stress tensor
σ_{st}	Limiting stress determining transition to plasticity
σ_{22}^{ini}	Initial stress within proppant
τ_y	Yield stress of fracturing fluid
φ	Proppant pack porosity

$$\frac{p^{(2)} + p_{\text{pl}}}{\text{erf}\left(\chi/2\sqrt{\kappa^{(1)}}\right)} \exp\left[-\left(\frac{\chi}{2\sqrt{\kappa^{(1)}}}\right)^2\right] + \frac{p_{\text{pl}}}{1 - \text{erf}\left(\chi/2\sqrt{\kappa^{(2)}}\right)}\sqrt{\frac{\kappa^{(1)}}{\kappa^{(2)}}}\exp\left[-\left(\frac{\chi}{2\sqrt{\kappa^{(2)}}}\right)^2\right] = \frac{\chi\eta\beta p_{\text{pl}}\sqrt{\pi\kappa^{(1)}}}{2k}\left[\frac{1}{E_{3333}} - \frac{1}{(K + 4G/3)}\right]. \tag{71}$$

Numerical solution to this equation allows finding χ, which, in turn, allows finding the variation of the pressure in the layer $0 \leq x_3 \leq x_3^{(1)}$ in the form:

$$p^{(1)} = p^{(2)} + \left(p_{\text{pl}} - p^{(2)}\right)\text{erf}\left(\frac{x_3}{2\sqrt{\kappa^{(1)} t}}\right)\left[\text{erf}\left(\frac{\chi}{2\sqrt{\kappa^{(1)}}}\right)\right]^{-1}.$$

For $x_3^{(1)} \leq x_3 \leq \infty$, the pore pressure varies according to the law

φ_0	Initial fracture porosity
φ_a	Internal friction angle
φ_e	Porosity adjusted of elastic zone
φ_{pl}	Porosity adjusted for deformation
φ_r	Rock porosity
χ	Self-similar coordinate
ρ	Density
ρ_i^f	Fluid porosity of i-th phase
$\rho_{i,0}^f$	Initial fluid porosity of i-th phase

Latin symbols

a	Difference between plastic zone length and length of zone between pillars
A_s	Compaction coefficient
b	Length of the plastic flow zone
B_f	Formation volume factor
c	Cohesion
c_0	Initial cohesion
C_{FD}	Dimensionless fracture conductivity
C_{FD}^0	Initial dimensionless conductivity
$C_{k,i}$	Fracture permeability to initial fracture permeability ratio at the i-th cell
C_L	Carter leak-off coefficient
$C_{w,i}$	Fracture aperture to initial fracture aperture ratio at the i-th cell
C'	Kozeny-Carman constant
D	Time-differentiation operator d/dt
e_0	Dimensionless depth of embedment
E	Young modulus
E_{ijkl}	Coefficient in dependence between stress and deformation
E_s	Young modulus of rock
G	Shear modulus of proppant pack
G_s	Shear modulus of rock
h	Depth of rock
H	Plastic strengthening modulus
H_f	Rheology coefficient
J_d	Dimensionless productivity index
k_i	Relative permeability of i-th phase
$k_{(i)}$	Fracture permeability at the i-th cell
$k_{(0,i)}$	Initial fracture permeability at the i-th cell
k_{ij}	Permeability at the i-th cell
$k_{f,0}$	Initial fracture permeability
k_r	Rock permeability
K	Bulk compression modulus
K_f	Fluid bulk modulus
K_{Jd}	The ratio of dimensionless well productivity with geomechanical effects to that with no geomechanics effects
K_s	Bulk modulus of the matrix
l	Length of zone filled by fluid between proppant pillars
L	Fracture length
M	Biot module
n	Power in equation for Bingham rheology
N	Total number of grains
N_k	Reservoir permeability to initial fracture permeability ratio
N_{ns}	Number of nodes
N_g	Fracture length to initial fracture aperture ratio
N_{Sh}	Dimensionless time, Strouhal number
N_y	Dimensionless critical gradient
p_d	Pressure acting of proppant
p_h	Hydraulic fracturing pressure
p_{pl}	Constant pressure at the boundary of the plasticity zone
p_{si}	Pressure in fracture
p_r	Pore pressure
p_{wf}	Bottomhole pressure
Δp	Pressure gap in zone of plastic deformation
Δp_d	Magnitude of pressure decline
Δp_h	Confinement stress of the walls
Δp_{max}	Constant in formula for pressure
Δp_s	Threshold pressure drop
Δp_w	Initial pressure gap in fracture
Δp_1	Pressure decline
p_0	Initial pressure in fracture
p_1	Constant pressure
p_2	Bottomhole pressure
$p^{(1)}$	Pressure within the domain of plastic rock deformations
$p^{(2)}$	Pressure outside the domain of plastic rock deformations
p^s	Pressure on s-th iteration
p^*	Dimensionless pressure
q_i^m	Mass transfer rate
q_i	Influx of i-th phase
Q	Liquid flowrate
$Q_{2h}, Q_{1d/7d}$	Oil production in 2 h/1 day/7 days
ΔQ	Relative oil production
r	Radial coordinate with a centre in wellbore
r_e	External boundary radius
r_p	Particle radius
r_w	Well radius
r'_w	Effective well radius
s_i	Saturation of i-th phase
$s_{(o,i)}$	Oil saturation at the i-th cell
s_{ij}	Deviatoric part of the stress tensor
S_f	Skin factor
t	Time
T	Shear stress intensity
T_{drop}	Dimensionless time of pressure drop in wellbore
T_{sc}	Time scale
T_r	Relaxation time
u_i	Darcy velocity of i-th phase
U	Newtonian fluid velocity
U_0	Velocity scale
v	Displacement of the fracture faces
v_{max}	Maximum displacement of the fracture faces
v_{pl}	Velocity of the front of plasticity
w	Fracture aperture
w_{ij}	Relative aperture at the i-th cell
$w_{(i)}$	Fracture aperture at the i-th cell
w_0	Initial fracture aperture
$w_{(0i)}$	Initial fracture aperture at the i-th cell
x	Coordinate alongside fracture
x_f	Initial fracture length
x_{cf}	Effective fracture length
x_i	Node coordinate in the modelling mesh
x_1	Coordinate alongside fracture
x_2	Coordinate perpendicular to fracture
Δx	Size of mesh cells in flowback model
Δx_1	Length of the element of hydraulic fracture
$y_{b,i}$	Bottomhole coordinate over the fracture height axis at the i-th cell
$y_{t,i}$	Top coordinate over the fracture height axis at the i-th cell

References

Abbasi, M.A., Dehghanpour, H., Hawkes, R.V., 2012. Flowback analysis for fracture characterization. In: SPE Canadian Unconventional Resources Conference. https://doi.org/10.2118/162661-MS.

Adachi, J., Siebrits, E., Peirce, A., Desroches, J., 2007. Computer simulation of hydraulic fractures. Int. J. Rock Mech. Min. Sci. 44, 739–757. https://doi.org/10.1016/j.ijrmms.2006.11.006.

Aksenov, V., Chertov, M., Sinkov, K., 2021. Application of accelerated fixed-point algorithms to hydrodynamic well-fracture coupling. Comput. Geotech. 129, 103783. https://doi.org/10.1016/j.compgeo.2020.103783.

Al-Fariss, T., Pinder, K., 1987. Flow through porous media of a shear-thinning liquid with yield stress. Can. J. Chem. Eng. 65, 391–405. https://doi.org/10.1002/cjce.5450650306.

Basniev, K.S., Dmitriev, N.M., Chilingar, G.V., Gorfunkle, M., Nejad, A.G.M., 2012. Mechanics of Fluid Flow. John Wiley & Sons.

Bird, R.B., 2002. Transport phenomena. Appl. Mech. Rev. 55, R1–R4. https://doi.org/10.1115/1.1424298.

Carman, P.C., 1937. Fluid flow through granular beds. Trans. Inst. Chem. Eng. 15,

150–166.

Carter, R., 1957. Derivation of the general equation for estimating the extent of the fractured area. In: Howard, G.C., Fast, C.R. (Eds.), Appendix I of "Optimum Fluid Characteristics for Fracture Extension", Drilling and Production Practices. American Petroleum Institute, New York, USA, pp. 261–269.

Chertov, M., Sinkov, K., 2020. On numerical simulation of cascading failure of hydraulic fractures due to aggressive flowback. In: 54th US Rock Mechanics/Geomechanics Symposium.

Chuprakov, D., Belyakova, L., Iuldasheva, A., Alekseev, A., Syresin, D., Chertov, M., Spesivtsev, P., Salazar Suarez, F.I., Velikanov, I., Semin, L., et al., 2020. Proppant flowback: can we mitigate the risk?. In: SPE Hydraulic Fracturing Technology Conference and Exhibition https://doi.org/10.2118/199748-MS.

Chuprakov, D., Iuldasheva, A., Alekseev, A., 2021. Criterion of proppant pack mobilization by filtrating fluids: theory and experiments. J. Petrol. Sci. Eng. 196, 107792. https://doi.org/10.1016/j.petrol.2020.107792.

Cinco-Ley, H., et al., 1981. Transient pressure analysis: finite conductivity fracture case versus damaged fracture case. In: SPE Annual Technical Conference and Exhibition. https://doi.org/10.2118/10179-MS.

Dahi Taleghani, A., Cai, Y., Pouya, A., 2020. Fracture closure modes during flowback from hydraulic fractures. Int. J. Numer. Anal. Methods GeoMech. 44, 1695–1704. https://doi.org/10.1002/nag.3086.

Dana, A., Zheng, Z., Peng, G.G., Stone, H.A., Huppert, H.E., Ramon, G.Z., 2018. Dynamics of viscous backflow from a model fracture network. J. Fluid Mech. 836, 828. https://doi.org/10.1017/jfm.2017.778.

Desroches, J., Bratton, T., 2000. Formation characterization: well logs. In: Economides, M., Nolte, K. (Eds.), Reservoir Stimulation, third ed. Wiley.

Detournay, E., Cheng, A.H.D., 1993. Fundamentals of poroelasticity. In: Fairhurst, C. (Ed.), Analysis and Design Methods. Pergamon, Oxford, pp. 113–171. https://doi.org/10.1016/B978-0-08-040615-2.50011-3.

d'Huteau, E., Gillard, M., Miller, M., Peña, A., Johnson, J., Turner, M., Medvedev, O., Rhein, T., Willberg, D., 2011. Open-channel fracturing—a fast track to production. Oilfield Rev. 23, 4–17.

Ding, X., Zhang, G., Zhao, B., Wang, Y., 2017. Unexpected viscoelastic deformation of tight sandstone: insights and predictions from the fractional maxwell model. Sci. Rep. 7, 1–11. https://doi.org/10.1038/s41598-017-11618-x.

Diyashev, I.R., Economides, M.J., 2006. The dimensionless productivity index as a general approach to well evaluation. SPE Prod. Oper. 21, 394–401. https://doi.org/10.2118/94644-PA.

Dontsov, E., Boronin, S., Osiptsov, A., Derbyshev, D.Y., 2019. Lubrication model of suspension flow in a hydraulic fracture with frictional rheology for shear-induced migration and jamming. Proceedings of the Royal Society A 475, 20190039. https://doi.org/10.1098/rspa.2019.0039.

Dugdale, D.S., 1960. Yielding of steel sheets containing slits. J. Mech. Phys. Solid. 8, 100–104. https://doi.org/10.1016/0022-5096(60)90013-2.

Economides, M., Nolte, K. (Eds.), 2000. Reservoir Stimulation, third ed. John Wiley & Sons, Chichester, UK.

Erofeev, A., Nikitin, R., Mitrushkin, D., Golovin, S., Baykin, A., Osiptsov, A., Paderin, G., Shel, E., 2019. Cyber frac—software platform for modeling, optimization and monitoring of hydraulic fracturing operations (Russian). Neftyanoe khozyaystvo-Oil Industry 2019 64–68. https://doi.org/10.24887/0028-2448-2019-12-64-68.

Filippov, D.D., Vasekin, B.V., Maksimov, D.Y., Mitrushkin, D.A., Mezentseva, M.A., Shcherbina, V.V., Roshchektayev, A.P., et al., 2020. Novel approach to detailed flow modeling in fractured reservoirs using adaptive pebi grids. In: SPE Russian Petroleum Technology Conference. https://doi.org/10.2118/201960-MS.

Fu, Y., Dehghanpour, H., 2022. Advances in flowback analysis: fracturing water production obeys a simple decline model. In: Unconventional Shale Gas Development. Elsevier, pp. 299–321. https://doi.org/10.1016/B978-0-323-90185-7.00003-0.

Guo, S., Wang, B., Li, Y., Hao, H., Zhang, M., Liang, T., 2022. Impacts of proppant flowback on fracture conductivity in different fracturing fluids and flowback conditions. ACS Omega 7, 6682–6690.

Gupta, S.C., 2017. The Classical Stefan Problem: Basic Concepts, Modelling and Analysis with Quasi-Analytical Solutions and Methods, vol. 45. Elsevier.

Ishlinsky, A.Y., 1968. Comparison of two models of crack propagation in a solid body [in Russian]. Proc. Acad. Sci. USSR.Mech.solid body 168–177.

Jia, P., Ma, M., Cao, C., Cheng, L., Yin, H., Li, Z., 2022. Capturing dynamic behavior of propped and unpropped fractures during flowback and early-time production of shale gas wells using a novel flow-geomechanics coupled model. J. Petrol. Sci. Eng. 208, 109412. https://doi.org/10.1016/j.petrol.2021.109412.

Kachanov, M., Tsukrov, I., Shapiro, B., 1994. Effective moduli of solids with cavities of various shapes. Appl. Mech. Rev. 47, S151–S174. https://doi.org/10.1115/1.3122810.

Katende, A., O'Connell, L., Rich, A., Rutqvist, J., Radonjic, M., 2021. A comprehensive review of proppant embedment in shale reservoirs: experimentation, modeling and future prospects. J. Nat. Gas Sci. Eng., 104143 https://doi.org/10.1016/j.jngse.2021.104143.

Lamidi, A.L.B., Clarkson, C.R., 2022. A rigorous coupled flow-geomechanics semi-analytical approach for analyzing early flowback data from multifractured horizontal wells with complex fracture geometry. In: SPE Hydraulic Fracturing Technology Conference and Exhibition. https://doi.org/10.2118/209114-MS.

Lecampion, B., Bunger, A., Zhang, X., 2018. Numerical methods for hydraulic fracture propagation: a review of recent trends. J. Nat. Gas Sci. Eng. 49, 66–83. https://doi.org/10.1016/j.jngse.2017.10.012.

Li, X.Y., Gu, S.T., He, Q.C., Chen, W.Q., 2013. Penny-shaped dugdale crack in a transversely isotropic medium and under axisymmetric loading. Math. Mech. Solid 18, 246–263. https://doi.org/10.1177/1081286512437395.

Moussa, T., Barhaug, J., Witt, D., Hawkes, R., Dehghanpour, H., 2022. Linking flowback recovery to completion efficiency: Niobrara-dj basin case study. In: SPE Hydraulic Fracturing Technology Conference and Exhibition. https://doi.org/10.2118/209136-MS.

Osiptsov, A., 2007. Asymptotic models of solidification in cooling thin-layer flows of a highly viscous fluid. Fluid Dynam. 42, 170–183. https://doi.org/10.1134/S0015462807020032.

Osiptsov, A., 2017. Fluid mechanics of hydraulic fracturing: a review. J. Petrol. Sci. Eng. 156, 513–535. https://doi.org/10.1016/j.petrol.2017.05.019.

Osiptsov, A., Boronin, S., Zilonova, E., Desroches, J., 2018. Managed saffman-taylor instability during overflush in hydraulic fracturing. J. Petrol. Sci. Eng. 162, 513–523. https://doi.org/10.1016/j.petrol.2017.10.018.

Osiptsov, A., Garagash, I., Boronin, S., Tolmacheva, K., Lezhnev, K., Paderin, G., 2020. Impact of flowback dynamics on fracture conductivity. J. Petrol. Sci. Eng. 188, 106822. https://doi.org/10.1016/j.petrol.2019.106822.

Osiptsov, A., Vainshtein, A., Boronin, S., Faizullin, I., Paderin, G., Shurunov, A., Uchuev, R., Garagash, I., Tolmacheva, K., Lezhnev, K., Prunov, D., Chebykin, N., 2019. Towards field testing of the flowback technology for multistage-fractured horizontal wells: modeling-based design and practical implications. In: SPE Russian Petroleum Technology Conference. https://doi.org/10.2118/196979-MS.

Potapenko, D., Theuveny, B., Williams, R., Moncada, K., Campos, M., Spesivtsev, P., Willberg, D., et al., 2019. State of the art of flow management for frac plug drillout and flowback. In: SPE Annual Technical Conference and Exhibition. https://doi.org/10.2118/196084-MS.

Potapenko, D., Theuveny, B., Williams, R., Moncada, K., Campos, M., Spesivtsev, P., Willberg, D., et al., 2020. Protect wells during frac plug drillouts and well flowback operations for hydraulically fractured wells—the state of the art in 2020. In: Abu Dhabi International Petroleum Exhibition & Conference. https://doi.org/10.2118/203221-MS.

Potapenko, D.I., Williams, R.D., Desroches, J., Enkababian, P., Theuveny, B., Willberg, D.M., Moncada, K., Deslandes, P., Wilson, N., Neaton, R., Mikovich, M., Han G.,C., Y., 2017. Securing long-term well productivity of horizontal wells through optimization of postfracturing operations. In: SPE Annual Technical Conference and Exhibition. https://doi.org/10.2118/187104-MS.

Redekop, E., Boronin, S., Tolmacheva, K., Burukhin, A., Osiptsov, A., Belonogov, E., 2021. Effects of salinity and rock clogging on injectivity dynamics of flooding wells: experiments, modeling and validation on field data. J. Petrol. Sci. Eng. 202, 108504. https://doi.org/10.1016/j.petrol.2021.108504.

Rudnicki, J.W., Rice, J., 1975. Conditions for the localization of deformation in pressure-sensitive dilatant materials. J. Mech. Phys. Solid. 23, 371–394. https://doi.org/10.1016/0022-5096(75)90001-0.

Skopintsev, A., Dontsov, E., Baykin, A., Golovin, S., 2022. The influence of heterogeneous proppant pack on fracture closure and productivity. J. Petrol. Sci. Eng. 214, 110494. https://doi.org/10.1016/j.petrol.2022.110494.

Sneddon, I.N., 1946. The distribution of stress in the neighbourhood of a crack in an elastic solid. Proc. Roy. Soc. Lond. Math. Phys. Sci. 187, 229–260. https://doi.org/10.1098/rspa.1946.0077.

Vainshtein, A., Fisher, G., Boronin, S., Osiptsov, A., Faysullin, I., Paderin, G., Shurunov, A., Prutsakov, A., Uchuev, R., Garagash, I., Tolmacheva, K., Shel, E., Prunov, D., Chebykin, N., 2020. Field testing of the flowback technology for multistage-fractured horizontal wells: test results and primary interpretation of the results. In: SPE Russian Petroleum Technology Conference. https://doi.org/10.2118/202056-MS.

Vainshtein, A., Fisher, G., Strizhnev, G., Boronin, S., Osiptsov, A., Abdrakhmanov, I., Paderin, G., Prutsakov, A., Uchuev, R., Garagash, I., Tolmacheva, K., Shel, E., Prunov, D., Chebykin, N., Fayzullin, I., 2021. Field testing of the flowback technology for multistage-fractured horizontal wells: generalization to find an optimum balance between aggressive and smooth scenarios. In: SPE Russian Petroleum Technology Conference. https://doi.org/10.2118/206635-MS.

Valov, A., 2021. On the simultaneous growth of multiple hydraulic fractures emanating from an inclined well. In: Journal of Physics: Conference Series. IOP Publishing, 012079. https://doi.org/10.1088/1742-6596/2057/1/012079.

Verdugo, M., Doster, F., 2022. Impact of capillary pressure and flowback design on the clean up and productivity of hydraulically fractured tight gas wells. J. Petrol. Sci. Eng. 208, 109465. https://doi.org/10.1016/j.petrol.2021.109465.

Wang, J., Elsworth, D., 2018. Role of proppant distribution on the evolution of hydraulic fracture conductivity. J. Petrol. Sci. Eng. 166, 249–262. https://doi.org/10.1016/j.petrol.2018.03.040.

Wang, J., Elsworth, D., Denison, M.K., 2018. Propagation, proppant transport and the evolution of transport properties of hydraulic fractures. J. Fluid Mech. 855, 503–534. https://doi.org/10.1017/jfm.2018.670.

Wijaya, N., Sheng, J.J., 2020. Surfactant selection criteria with flowback efficiency and oil recovery considered. J. Petrol. Sci. Eng. 192, 107305. https://doi.org/10.1016/j.petrol.2020.107305.

Witherspoon, P.A., Wang, J.S., Iwai, K., Gale, J.E., 1980. Validity of cubic law for fluid flow in a deformable rock fracture. Water Resour. Res. 16, 1016–1024. https://doi.org/10.1029/WR016i006p01016.

You, L., Zhang, N., Kang, Y., Xu, J., Cheng, Q., Zhou, Y., 2021. Zero flowback rate of hydraulic fracturing fluid in shale gas reservoirs: concept, feasibility, and significance. Energy Fuels 35, 5671–5682.

Zhang, F., Emami-Meybodi, H., 2020a. Flowback fracture closure of multi-fractured horizontal wells in shale gas reservoirs. J. Petrol. Sci. Eng. 186, 106711. https://doi.org/10.1016/j.petrol.2019.106711.

Zhang, F., Emami-Meybodi, H., 2020b. A semianalytical method for two-phase flowback rate-transient analysis in shale gas reservoirs. SPE J. 25, 1599–1622. https://doi.org/10.2118/201225–PA.

Zhang, F., Emami-Meybodi, H., 2021. Analysis of early-time production data from multi-fractured shale gas wells by considering multiple transport mechanisms through nanopores. J. Petrol. Sci. Eng. 197, 108092. https://doi.org/10.1016/j.petrol.2020.108092.

Zhang, F., Emami-Meybodi, H., 2022a. Semianalytical method of two-phase liquid transport in shale reservoirs and its application in fracture characterization. AIChE J. 68, e17449. https://doi.org/10.1002/aic.17449.

Zhang, F., Emami-Meybodi, H., 2022b. A type-curve method for two-phase flowback analysis in hydraulically fractured hydrocarbon reservoirs. J. Petrol. Sci. Eng. 209, 109912. https://doi.org/10.1016/j.petrol.2021.109912.

Zhang, Q., Taleghani, A.D., 2022. On the role of proppants and geomechanics on flowback behavior in complex fracture networks. J. Petrol. Sci. Eng. 216, 110835. https://doi.org/10.1016/j.petrol.2022.110835.

Zheng, W., 2017. Laboratory and Discrete Element Study of Proppant Crushing and Embedment and Their Influence on Fracture Conductivity. Doctoral dissertation. University of British Columbia. https://doi.org/10.14288/1.0362394.